THESIS FOR THE DEGREE OF LICENTIATE OF ENGINEERING

INVESTIGATIONS OF WATERJET/HULL INTERACTION EFFECTS

Arash Eslamdoost

Investigations of Waterjet/Hull Interaction Effects
Arash Eslamdoost

Investigations of Waterjet/Hull Interaction Effects
Arash Eslamdoost
Department of Shipping and Marine Technology
Division of Ship Design
Chalmers University of Technology

ABSTRACT

A waterjet propulsor operates in a different way than a conventional propeller. This makes it hard to use the same concepts for studying the thrust and powering of these systems. The net thrust of the propeller can be obtained by measuring the force transmitted through its shaft, but since there is not just a single contact point between the waterjet unit and the hull, the net thrust measurement cannot be easily accomplished for the waterjet unit. Instead another thrust force, which is simpler to measure, is defined to express the magnitude of the waterjet unit thrust. The new thrust definition is called the gross thrust and is obtained by the measurement of the momentum flux change through the waterjet control volume. In this thesis, it has been tried to find out the links between these two thrust forces.

The original work fulfilled in this thesis can be divided in to two main parts. The first part is an introduction to an iterative algorithm for modelling the effect of the waterjet on the hull. The algorithm is called the Pressure Jump Method. This method is based on the fact that the resistance forces are balanced with the thrust force created by the head increase through the waterjet pump. In this thesis, the Pressure Jump Method is coupled with a potential flow solver capable of non-linear free-surface modelling but there is not any limitation for the method to be used in combination with, e.g., RANS solvers. Validation and verification of the Pressure Jump Method is accomplished by comparing the computational results with experimental data available from a test case. The second part of the thesis is dedicated to investigate the individual contribution of different parameters that may influence the thrust deduction of a waterjet-propelled craft. In this part the results obtained from the Pressure Jump Method along with some extra calculations are employed to find out the dominant parameters, which contribute to the thrust deduction.

Keywords: waterjet propulsion, waterjet/hull interaction, numerical simulation, potential flow, non-linear free-surface, pressure jump method, net thrust, gross thrust, thrust deduction, sinkage, trim angle

ii

PREFACE

This thesis presents the work carried out at the Hydrodynamics Group of the Department of Shipping and Marine Technology, Chalmers University of Technology during 2009 to 2012. It is in the framework of the PhD project "Investigations of Waterjet/Hull Interaction Effects," supported by Rolls-Royce Marine through the University Technology Centre in Computational Hydrodynamics hosted by the Department of Shipping and Marine Technology at Chalmers.

ACKNOWLEDGEMENTS

TABLE OF CONTENTS

1 Introduction

Waterjet propulsion may be considered as one of the common contemporary propulsion systems. This propulsion method is not as popular as conventional propellers but is competitive to them in certain operating conditions The tendency to use waterjet propulsion is increasing thanks to the enhanced efficiency of these systems. In order to investigate the reasons behind this increased interest in applying waterjet propulsion, we need to know the specific characteristics of the propulsion method and its advantages and disadvantages under various operating conditions. In this chapter, a brief review of the history of waterjet propulsion developments is presented and then the components of current waterjet units and their features are introduced. The historical steps mentioned in this chapter are not covering the entire known progress in the history of waterjet propulsion but only some selected pieces to show the pace of the development.

1.1 History of Waterjet Propulsion Development

The very first idea of a mechanised marine propulsion system was introduced in England 's patent no. 5 by David Rumsey (1631). The first sign of employing steam power for industrial purposes emerges through this patent and Ramsey specifically mentions that steam power might be used "*to make boates, shippes and barges to goe against the wind and tyde*"[1].

In ancient times, an Archimedean screw (Figure 1.1) was being used to irrigate and pump out flooded ships. The concept used in this screw to pump water was more or less similar to the sketch drawn by Leonardo da Vinci showing a rotating spiral for raising water and the rotor of his famous helicopter (Figure 1.2). Adopting the Archimedian screw as a ship propeller, Toogood and Hays (1661) introduced an initial waterjet propulsion concept, which is registered as patent no. 132 in England with the following description:

"*A newe inventĉon of forceing water by bellowes, not done with wind, alsoe the draweing it vpp with leatheme baggs linked togeather in manner of bucketts where the bellowes cannot be placed which may be for the publique benefitt of shipping, drayning of mines, bringing water to houses, emptying of rivers or ponds, drayneing & watering of grounds, or any way of pumping water, together with a particular way of forceing water through the bottome or sides of shipps belowe the surface or toppe of the water which may be of singular vse and ease in navigaĉon, & was never before publiquely done or vsed within any of our kingdomes, Dominions, or Territories*"[2].

Years later, in 1730, Dr. John Allen, MD, introduced a different concept of waterjet propulsion, which generated steam aboard a vessel and discharged the steam jet through the stern into the water forcing the craft along [3].
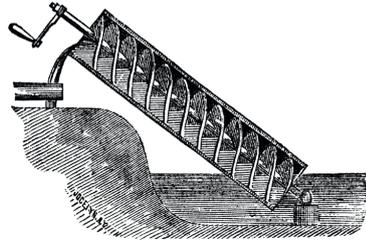
Figure 1.1. Archemidian screw
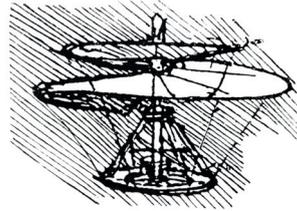
Figure 1.2. Helicopter drawing by Leonardo da Vinci

James Thomas Flexner [4] discusses the history of the steamboats, developers and patents in this area. He mentions that in 1753, Benjamin Franklin (1706-1790) was inspired by the Frenchman Daniel Bernoulli (1700-1782) to develop waterjet propulsion systems. Flexner says Bernoulli believed that *"if a stream of water was driven out of the stern of a boat below the water line, its reaction on the body of water in which the boat floated would drive the vessel forward. Bernoulli's experiment had merely involved an L-shaped pipe stretching to the rear into which water could be poured; Franklin added a pump that drew water in at the bow and drove it out at the stern. 'A fire engine might in some case be applied to this operation with advantage' he concluded"*.

In the mid-1780's and early 1790's, James Rumsey and John Fitch each separately developed waterjet propulsion systems. Rumsey developed a tube boiler and utilized it in his waterjet system, which consisted of a cylinder of steam on top and a pump cylinder, both sharing a single piston rod. Water was sucked through some valves placed in the keel and rushed out of the stern. Rumsey's waterjet system propelled the boat with the speed of two miles per hour, about 1.73 knots. In 1790, Fitch applied a same concept as introduced by Allen sixty years earlier, forcing a column of air through trunks filled with water out of the stern while the bow valves were closed [3]. Figure 1.3 illustrates a sketch of Fitch's design [5].
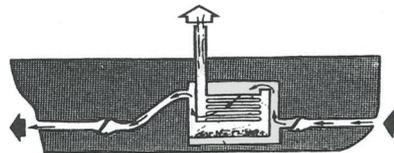
Figure 1.3. Sketch (by Schult) of Fitch's 1790 Waterjet Patent [5]

After some trials with different concepts of waterjet systems, engineers noticed that "certain characteristics of early waterjet proposals, such as the friction of the water

in the long pipes with the relatively inefficient combination of a positive displacement pump, coupled with a reciprocating steam engine, would not be able to match the efficiency of paddle wheels or screw propellers" [3]. The problems mentioned were solved to some extent by the invention of hydraulic pumps. Roy, 1994 [3], discusses the history of developing and utilizing hydraulic pumps. A rather developed design of waterjet systems including an hydraulic pump based on Barnaby's suggestion is depicted in Figure 1.4. Barnaby suggested to "reduce the efficiency losses by obviating the need to raise or turn the ducts of water and by aligning the axis of the centrifugal pump horizontally instead of vertically"; he also mentioned that "if the pump could be put outside the boat, there would be no problem with getting water into the boat and up to the pump, and, little or no water would be carried" [3].
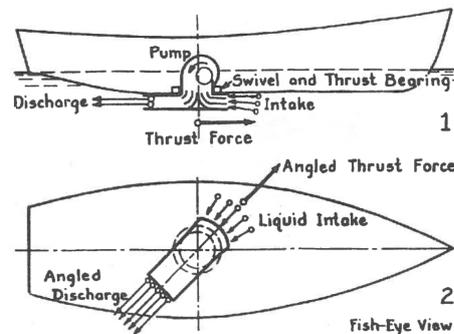
Figure 1.4 "Hydraulic-Jet" propulsion based on Barnaby's idea in 1884 [6]

Roy [3], indicates the Energy Burst Systems as the next important step towards modern waterjet systems. He believes that although Fitch's patent of 1790 was a waterjet system, it may be described as an intermittent energy burst waterjet propulsor. Another example of the early designs of energy burst systems in known as the McHugh (1916) pulsejet [3]. Although this pulsejet system was unsuccessful in full scale design but extremely effective in model scale and countless numbers were sold as toys from the 1920s and onwards [3]. Figure 1.5 shows a schematic presentation of a similar pulsejet system. There exists an engine consisting of a boiler connected to one or two tubes. By heating up the boiler, the steam inside expands and pushes the water column inside the tubes backwards, resulting in a thrust force. Next, due to the condensation of the steam bubble and lower pressure inside the boiler, water is sucked back into the tubes. This procedure continues repeatedly and causes a cyclical thrust force.
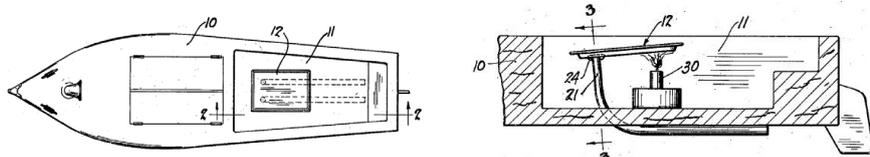
Figure 1.5 Diaphragm type of pulsejet engine [7]. The left figure shows the general arrangement of the system and the right figure depicts the side view of midsection of the pulsejet engine of diaphragm type. No. 12 and 30 show the boiler and heater respectively. Connected tubes are marked by no. 21.

Another example of more sophisticated energy burst waterjet systems is shown in Figure 1.6. In this design, "the ingenious power head utilized a reed valve at the air inlet to control the energy burst in the combustion gas exited through a novel ring-shaped device which acted as both a rudimentary pressure valve and a discharge nozzle" [3].

Figure 1.6 Sketch by Schult of H. J. MacCollum's (1946) Pulse Jet Outboard [5]

In 1950, Kenneth produced a small jet outboard with an horizontal impeller. In the same year, William Hamilton developed the very first high-speed jet propulsion system, which in general showed similarities with modern designs employed nowadays. After this time, some upgrades have been made on waterjet designs to increase the efficiency of these propulsion systems, which in some cases resulted in outstanding outcomes. An example of such an outcome is the 68 *m* Destriero which, propelled by three KaMeWa units [3], scored an Atlantic record at almost 53 knots. The history reviewed in this section only represented some selected designs and developments achieved in the history of waterjet propulsion systems. Some additional historical events related to marine waterjet development are provided in Appendix A. More detailed information may be found in Allison [8] and Roy [3].

1.2   Connection to other Turbomachines

The principle behind all types of conventional turbomachines is quite similar. These systems are either used to absorb energy from a fluid stream and deliver mechanical power through a shaft (e.g. windmills, water turbines) or employ the delivered power through a shaft to create a stream of higher energy levels (e.g. pumps, fans, axial compressors). Figure 1.7 shows the connection between different types of turbomachines in the form of a box model [9]. The characteristic properties of each face of the box model are mentioned in Table 1.1. By reviewing the development history of the thrusters, it is observed that when there is need for higher velocities, thrusters move from external flow to internal flow thrusters inside a special casing; this is similar to the development of aeronautical thrusters which started with propellers and were later upgraded to jet engines. A same trend is observed in marine thrusters, which were started with paddles and propellers and were then improved to become ducted propellers and waterjet propulsion systems.
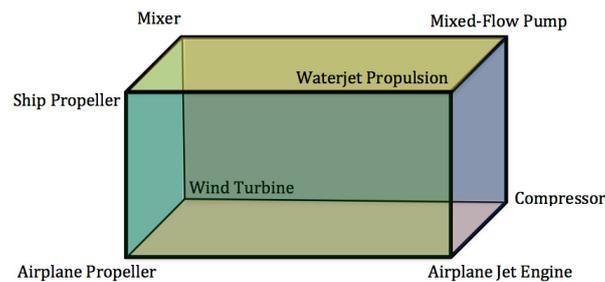
Figure 1.7 Relation between the waterjet propulsion systems and the other types of turbomachinery [9]

Table 1.1 Characteristics of the turbomachins on each face of the box model introduced in Figure 1.7

Front Face	Designed to produce thrust
Back Face	Any thrust production is an undesirable effect
Top Face	Operate in water; Cavitation might be important
Bottom Face	Operate in air; Compressibility might be important
Left Face	External flow machines; Thrust transmision only through shaft only
Right Face	Internal flow machines; Thrust transmission through both shaft and casing

1.2.1   Comparison with Marine Propellers

Perusing the history of marine propulsors, there has been a tendency to employ marine screw propellers rather than waterjet systems, the reason is that the design and production procedure of propellers were easier. But the introduction of more efficient pumps utilizable in waterjet systems in recent decades has changed the strong tendency of using screw propellers. Nowadays, there are specific

characteristics of waterjet propulsion systems that make them a better choice in comparison with conventional marine propellers, including higher achievable velocity, better manoeuvrability (e.g. zero speed docking, sideways movement with multiple jet installation and the possibility to stop quickly) and lower noise levels.

Due to the fact that there are no appendages, such as struts, rudders etc., the shallow draft of the system makes it possible to run the craft in shallow waters. However, by operating in this condition, mud and other debris might be sucked into the system and cause damage to the pump system. At high speeds, the appendage drag can achieve 20% of the bare hull drag [10]. There is indeed no such drag component for waterjets.

The extent of cavitation is rather different for propellers and waterjet systems. Due to increased pressure inside the waterjet system, cavitation occurs at higher velocities. Therefore, when conventional transcavitating and supercavitating propeller performance fall off, waterjets are better choices; surface piercing propellers and waterjet systems are more or less competitive. According to the heavier weight of waterjet units compared to conventional propellers, these systems become more efficient on larger crafts such as wave-piercing ferries [11].

Combining waterjets and propellers in the form of hybrid propulsion is also a possible option. In this case smaller propellers with lower noise and vibration levels are used for normal cruising, while a central waterjet system would be employed to boost the system to achieve higher speeds.

1.3   Common Waterjet Systems

Generally, four different basic types of waterjet propulsion systems exist (Figure 1.8). The major difference between these designs is the ducting channel geometry and the pump installation in these systems. The most conventional intake is a flush type intake in which the duct opening is almost parallel to the intake flow. For ram type intakes, the intake opening is normal to the intake flow.

flush intake

ram intake

planing scoop intake

scoop intake
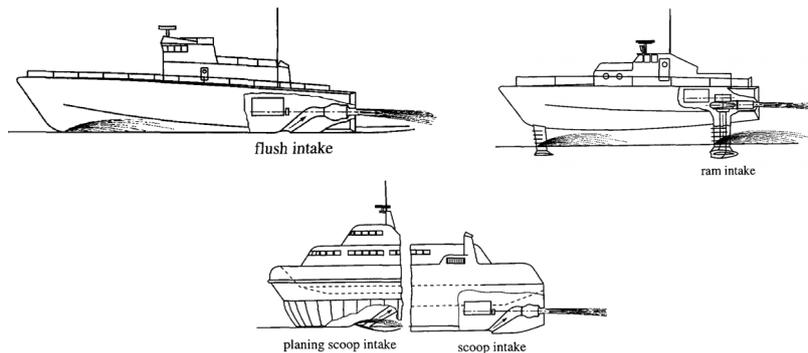
Figure 1.8 Basic intake concepts [12]

Figure 1.9 depicts the main components of flush intake waterjet system, which includes an inlet duct, pump, nozzle and steering unit. Water is sucked into the intake opening and guided through the ducting channel into the pump. As shown in Figure 1.10, pumps are categorized into to axial, mixed and centrifugal flow pumps based on the angle of inflow and outflow. Axial and mixed flow pumps are the major types being used in the design of waterjet propulsion systems. Generally, mixed flow pumps are wider compared to axial flow pumps; this should be taken into consideration during the design process, especially when multiple waterjet units are supposed to propel a vessel.

Passing through impeller and stator, the flow approaches the nozzle. The duty of a nozzle is to increase the momentum flux by ejecting the flow, which is accomplished by the contraction of the nozzle. "Nozzle is usually shaped such as to have the vena-contracta of the discharged jet coinciding with the nozzle exit" [10]. The vena-contracta of a jet is the section of the jet in which the average static pressure is identical to the ambient pressure in that section. Depending on the nozzle design, vena-contracta may occur at the nozzle discharge section or further downstream. Additional discussions about the position of vena-contracta take place in Section 'Vena-Contracta' of Chapter 3.
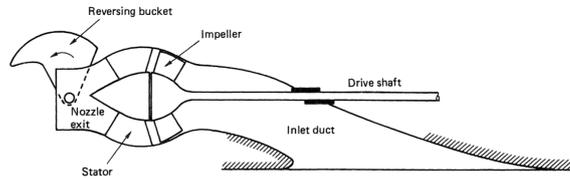
Figure 1.9 Typical waterjet general arrangement [11]
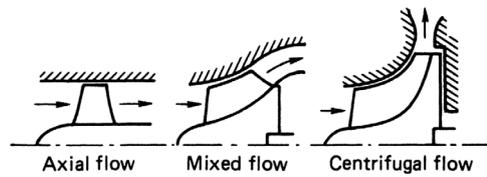
Figure 1.10 Pump impeller types [11]

Steering crafts propelled by waterjet systems is done either by means of a steerable nozzle (Figure 1.11) or by deflecting the direction of the discharged jet through some other installation. The angle through which the jet is directed would generally be of the order of ±30◦ [11]. Similarly, for stopping the vessel, flaps or a 'reversing bucket', is employed   which completely changes the direction of the jet momentum flux, as seen in Figure 1.11.
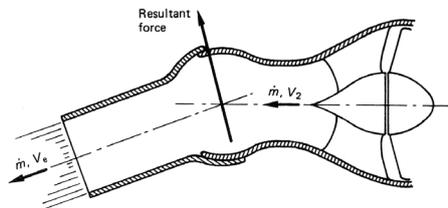
Figure 1.11 Principal of waterjet steering capability [11]

8

2 Literature Review and Motivation

2.1 Literature Review

In reviewing the research dedicated to understanding the behaviour of waterjet propulsion systems, many interesting papers and reports have been found that each in turn reveals facts about this propulsion method. In this chapter, a thorough review of the published literature in this area is presented. The summaries reviewed are presented in a chronological order below.

Purnell [13], raising the lower overall efficiency of the waterjet system comparing to that of propellers, discusses methods to increase the performance gains by using low momentum boundary layer flow for a wide flush intake on a waterjet propelled craft for producing the propulsion jet. The general concepts of boundary layer flow, such as boundary layer thickness, momentum velocity and energy velocity, are discussed in this report. Based on these parameters, a method of predicting pump size and overall waterjet system performance is highlighted. It is shown that applying a wider or large width/height intake area improves the overall propulsive coefficient.

Alexander et al. [14] performed full-scale towing and self-propulsion tests in order to determine the mechanisms of waterjet-hull interaction. They indicate that after-body pressure change due to the presence of the waterjet and jet system force component is the main reason responsible for the interaction. They point out that there exists an optimum trim angle for each hull and the forces and moments created by the jet system determine whether the trim angle of the self-propelled hull is smaller or bigger than the optimum trim angle.

Dyne and Lindell [15] question the method of obtaining the required net thrust from a thrust deduction fraction and instead introduced a direct method giving the shaft power without using any propulsive factor. Two different control volumes for obtaining the bare-hull and self-propelled viscous resistance directly from the momentum theorem are introduced. These viscous resistances are then applied to calculate the required net thrust to drive the vessel forward. Boundaries of the control volumes introduced are assumed to be far upstream and downstream of the hull where the flow is just in the axial direction. Moreover, for the sake of simplicity, the loss of the wake behind the model is assumed to be zero. For the bare-hull case, the wake is divided into two separate parts: First, a streamtube, which in the case of self-propulsion, passes through the ducting and the other part of the wake is a streamtube passing outside the ducting channel. The control volume applied to the self-propulsion case is slightly different and a part of the wake is passing through the ducting channel.

9

Roberts and Walker [16] studied the problem of boundary layer ingestion for waterjets and developed a two- dimensional theory for waterjet propulsion systems with and without boundary layer ingestion. Due to the development of a new boundary layer right after the intake, they show that boundary layer ingestion is not always beneficial. Besides, the effect of nozzle drag on the propulsive efficiency was investigated.

Through an analytical procedure, van Terwisga and Alexander [17] show that there is no intake drag for a flush type intake operating in a potential flow. Moreover, it is mentioned that the intake viscous drag in a viscous flow is negligibly small. It is stated that in case no longitudinal pressure gradient exists over the imaginary surface covering the intake opening, no interaction effect of the potential flow distortion by the hull on the jet performance may be detected. Finally, it is indicated that for a sufficiently large area around the flush intake, no net contribution of the intake-induced flow on the total lift force on jet-hull systems exists.

Johansson [18] studied the vertical force acting upon a marine waterjet propulsion unit and the way such forces change the trim angle and resistance of a planing craft. A numerical two-dimensional potential flow simulation was developed to investigate the pressure distribution around the waterjet. Two separate experimental tests were planned: One was confined to the intake geometry and the other was a self-propulsion test. Results from the intake test were incorporated into Savitsky's method of predicting the performance of a planing hull. Finally, it was noticed that no vertical force is created by the action of the waterjet unit but there is a bow-down trim variation due to the waterjet moment.

Kruppa et al. [18] in the 21st ITTC Waterjet Specialist Committee discussed possible power prediction methods for waterjet propulsion systems. Eventually, two different methods were proposed: First, the calculation of thrust force from momentum flux and the second is the direct measurement of thrust. The capture area width is here considered to be 30% larger than the intake width and its height is twice the boundary layer thickness at this section. A 20% error in the selected width of the rectangular cross section only result in 1% error of the power predicted. The method of calculating energy velocity at the capture area, as well as the outlet section of the jet is presented. Then, based on the obtained energy velocities, the momentum flux change at these sections is defined. Moreover, internal intake losses and scaling effects are also discussed. Due to different flow patterns around the bare hull and self-propelled case, it is stated that no general relationship between them could be found.

In his thesis work, van Terwisga [10] found that a difference between gross thrust and net thrust[*] may occur especially around ship speeds where the transom is not fully cleared. This difference is practically zero for higher speeds and therefore, the difference between gross thrust and bare hull resistance is a good measure of the resistance increment of the hull due to the waterjet-induced flow. Through an uncertainty analysis of propulsion tests, it was shown that that the error made in the flow rate measurement in power estimation increases with decreasing JVR. He divides the effects, which result in the resistance change of a self-propelled hull, into global and local effects. Global effects include the sinkage and trim of the hull, while a local effect is the change in the flow around the intake due to the ingested flow. Based on this classification, if the assumption of independence between the changes due to the local and the global flow is true, the change in resistance may be estimated from a linear development in a Taylor series. Based on the measurements of a powerboat propelled by a single waterjet unit, he concludes that the trim angle is the most important parameter for analysing the resistance increment of the hull.

Roberts [19] studied the effect of boundary layer ingestion in flush type waterjet intakes both experimentally and numerically. An experimental study was performed inside a wind tunnel using two different boundary layer thicknesses. The inflow capture streamtube was found to be essentially elliptical in cross-section. The measurement section was located 20% of the intake length in front of the intake tangency point. The width varied from 1.7 times the physical width of the intake for thin boundary layers up to twice the intake width for thick boundary layers. According to this finding, the recommended 21st ITTC [20] intake width, 1.3 times of the physical width of the intake, was questioned and he concluded that applying ITTC's recommended width might result in an over prediction of inflow momentum flux by 8.0% for a typical high speed ferry design which consequently results in gross thrust under prediction by 9.3%.

Allison et al. [8] studied the interaction of jet, free-surface, hull flow, and hull to investigate the resulting forces and moments through both CFD simulations and model tests. Based on a control volume for a hull with submerged nozzles and a reference frame moving with the hull, an analytical method to define inlet/hull flows for a large semi-displacement mono-hull was presented. The unmixed jet was treated as an equivalent flap with width equal to the width of the jet. The resulting lift force of the flaps was incorporated into force and moment equilibrium of the ship.

Hu and Zangeneh [21] compared single blade-to-blade channel model and whole impeller model to investigate the flow field in the impeller and nozzle of a waterjet

---

[*] Definition of gross thrust and net thrust are given in Chapter 3.

pump. Besides studying the effect of non-uniform inlet velocity on the impeller shaft torque, waterjet thrust calculation accuracy was analysed. Calculating the velocity distribution at the nozzle outlet and comparing its bulk average to the actual momentum velocity, an error of 0.4% in the jet momentum was reported.

van Terwisga et al. [22] in the 23rd ITTC Waterjet Specialist Committee try to define a standard test procedure for waterjet systems. General comments are provided on the design procedure of waterjet elements, such as intake and pump, and the procedure to investigate the waterjet hull interaction. In order to calculate the momentum and energy flux, a different formulation is introduced compared to the formulation adopted by the 21st ITTC. In the former formulation, pressure terms are included in the definition of momentum and energy flux, which in fact is not consistent with generally accepted definitions. Referring to the 21st ITTC Waterjet Specialist Committee Report [20] and van Terwisga [10], the problem of power estimation due to error in flow rate prediction was highlighted. Intake velocity profile, as well as shape and size of the capture area were also discussed in this report. It was concluded that an imaginary rectangular capture area with a width 1.3 times larger than the waterjet intake width may be a fair estimation. However, because of the conclusion made by Roberts [23], who claimed that the choice of rectangular capture area may lead to an under prediction of gross thrust by some 10%, it was suggested the exact shape of capture area should be obtained through CFD simulations. Considering the boundary layer thickness and scale effects, it is shown that the non-dimensional capture area in model scale is larger compared to the full scale. Moreover, considering the scale effects, the procedure to determine the tow force of the model test was discussed as well as general characteristics of the hull and corresponding waterjet geometry selected for model tests

Wilson et al. [24] present LDV measurements of velocities for the flow around a high speed hull form. Moreover, by means of static pressure taps, the static pressure coefficient was measured at different locations on the aft portion of the model hull. To accurately determine waterjet inlet momentum flux values, a correlation of CFD-determined pressure and velocities and LDV measurements coupled with a few hull static pressure taps is proposed. Rectangular, elliptical and scalloped (bottom part rectangular, top part elliptical) shapes were tried to specify the capture area. According to the measured wake factor, although the scalloped capture area seemed to conform best to the typical shape of the observed configuration, a simple rectangular assumption seems probably to be good enough.

Bulten and van Esch [25], by applying a RANS solver, obtained streamtubes of ducted propellers and waterjets. Neglecting the pressure, which acts on the streamtube surface, the thrust of these propulsion units based on the momentum balance for the defined streamtube was investigated. By introducing an artificial

diffuser concept, they tried to explain the contribution of the pressure force on the streamtube to the total thrust of the waterjet system.

Wilson et al. [26] performed a waterjet propulsion test on a slender high-speed hull form model propelled by four side-by-side waterjet units. Based on the 21st ITTC Waterjet Specialist Committee recommendations [20], the jet system thrust was calculated from the momentum flux change through the waterjet system control volume. Besides, some numerical investigations for both bare hull and self-propelled hull were made by means of a potential flow code capable of capturing the free surface. Waterjet intakes were represented by a flat rectangular segment of hull surface having a uniform normal velocity and sucking the flow inside the hull. A downward force was created on the aft-body of the hull due to the suction of the waterjets. This force grew larger by increasing the suction. A more detailed analysis of the balance of pressure and viscous forces on the ship aft body was suggested in order to explain the mechanism of negative thrust deduction. According to the larger Reynolds number of the ship compared to the model scale, the average velocity at the capture area in full scale will be higher than the model value. In full scale, both the non-dimensional flow rate and the jet velocity are therefore expected to increase. In order to take this increase into account, Wilson et al. employed a systematic scaling procedure proposed by Scherer [27].

van Terwisga et al. [28] on the 24th ITTC Specialist Committee on Waterjets present a comprehensive review of earlier studies on waterjet systems and ITTC standard method for waterjet system analysis. This report covers the earlier Committee suggestions including some modifications. Because of some practical difficulties inherent in direct thrust measurement, this method was off-the-list of the Committee and instead they focused on the momentum flux method. Powering characteristics and the efficiency of the whole waterjet system and its elements are also discussed. Separate interaction terms are then introduced for momentum, energy, thrust and drag. Formulations for obtaining the delivered thrust and corresponding power required through conservation laws of momentum and energy are articulated. Two different thrust deduction fractions are introduced, one relating bare hull resistance to net thrust, the other expressing the relationship between gross thrust and net thrust. The sum of these thrust deduction fractions is set to be equal to the total thrust deduction fraction. By introducing a correction factor for momentum velocity at the capture area, a formulation for obtaining a change in momentum flux is presented. In the absence of any detailed information about the capture area, an elliptical capture area 1.5 times wider than the geometrical intake width is recommended. More over, it is mentioned that just the intake centreline boundary layer profile will be sufficient while employing an elliptical capture area. The procedure for scaling the data obtained from the model scale to the full scale is

13

also presented. Finally, results of self-propulsion tests both on bare hull and self-propelled hull are presented and discussed.

Bulten [9] studied the flow inside waterjet propulsion systems employing CFD tools. Indicating the non-uniform velocity field at the pump section, different reasons were introduced as the causes of this non-uniformity. Non-uniform velocity distribution just before the intake due to the developing boundary layer, passing through the bend inside the ducting channel and the rotating shaft, were cited as the main cause of the flow non-uniformity at the pump inlet section. Three separate steps were taken to model the waterjet flow. First, the flow inside the ducting channel was modeled to obtain the non-uniform flow field just before the pump section. In order to investigate the effect of uniform and non-uniform flows at the pump inlet section, the flow inside the pump was modeled by employing both a quasi-state multiple frame of reference (MFR) method and a fully transient moving mesh method. Both these methods predicted almost the same head and power. Studying the unsteady forces on the impeller due to rotor-stator interaction it was shown that the magnitude of the radial interaction force depended on the flow rate though the pump. Eventually, both validated numerical models of the inlet and the pump were combined to simulate the complete waterjet installation. The integration of axial force component on the solid wall with a simplified version of the integral momentum balance equation was applied to calculate the thrust. A clear deviation between the results of these methods was reported for higher ship speeds. Also, a large vertical force was reported at the same range of speed. According to these findings, Bulten concluded that the method based on the momentum balance for the streamtube control volume was incorrect possibly because of the influence of the hull in the vicinity of the waterjet inlet and partly because of neglecting the contributions of the pressure distribution acting on the streamtube.

A comprehensive measurement campaign was completed by the Commercial Deployment of Transportation Technologies (CCDoTT) [29] on a demi-hull with a pair of waterjet units. The data presented in this report can be used to validate numerical simulations. The difference of boundary layer thickness due to scale change was taken into account in the data scaling procedure. Consequently, although the thrust deduction fraction was positive in the model scale, taking this correction into account resulted in a negative thrust deduction fraction. This conclusion raises the question of whether the thrust deduction is dependent on scaling or not.

Jessup et al. [30] accomplished a comprehensive set of experiments applying LDV and pitot-static tubes to investigate the velocity field and static pressure for three hull variants to study the effect of different propulsors. The first hull design was adapted to four propellers with open shaft and strut appendages. The second and

14

third hull designs were intended for axial and mixed flow waterjets. Hulls designed for axial flow waterjets normally have a narrower and shallower transom compared to hull designs for mixed flow waterjets. Although the overall thrust of the axial flow waterjet unit was smaller compared to the mixed flow waterjet unit, a negative thrust deduction fraction was reported for the hull with mixed flow waterjet units.

Hino and Ohashi [31] applied CFD analysis to free surface flow around a waterjet propelled ship. An actuator disk with a constant body force distribution was employed to model the propulsor. The sinkage and trim angle of the hull were fixed during the computation due to the measured data obtained from experiment. Doing a backward trace of streamlines from the actuator disk plane, they found out that the capture area was twice as wide as that of the intake duct; almost 30% larger than the ITTC recommended value.

Skipping the detailed flow modelling inside the ducting channels, Kandasamy et al. [32] derived an integral force/moment waterjet model and applied it to a CFD code to predict ship local flow and powering. In order to circumvent the difficulties of obtaining the intake capture area of the waterjet system, a control volume other than the control volume proposed by ITTC was applied for balancing force and moment. The maximum error of the simulated cases compared to experimental data was for the trim angle of the bare hull and self-propelled hull, which was almost 14% on the average. Although the predicted resistance error for the bare hull and self-propelled hull was less than 5%, the calculated thrust deduction fraction showed a larger deviation from the data measured.

Through the URANS approach and applying body force to model the pump effect, Takai [33] solved and analysed flow fields for bare hull and self-propelled high-speed sea lift hull over a speed range. Moreover, duct shape optimisation was accomplished in two separate stages. The upper curvature and lip shape modification reduced mainly minor pressure loss. Next, some effort was made to reduce the major loss principally due to friction drag in duct. Therefore, duct intakes were merged into each other in order to reduce the surface area of the intakes. Computational results based on the latter optimised intake showed improvement in inlet efficiency.

Ding and Wang [34] state that by applying conventional methods, intake loss is overestimated which results in overestimation of overall power. To overcome this problem, they introduce a method to determine the waterjet system flow loss by means of CFD. In this method, by dividing the surface between the internal flow ingested into the inlet duct and the external flow beneath the hull, an attempt to capture a virtual stream-tube is made. Based on the obtained stream-tube, the flow loss is calculated according to the difference of total head between the duct outlet

15

and the capture area ahead of the intake. They showed that the flow loss coefficient is approximately in the range of 0.05 to 0.12 for typical flush-type inlet duct, which is less than the empirical value of 0.2 to 0.3. Moreover, they mention that the shaft had a big influence on the flow loss.

2.2   Motivation

As seen in the literature review the physics behind the waterjet/hull interaction is not fully understood. A particularly interesting effect, which has intrigued the hydrodynamicists for a long time, is the negative thrust deduction reported for several hulls. Since this is of great importance for the waterjet design, one of the leading manufacturers of waterjet systems, Rolls-Royce AB in Sweden, proposed a project on waterjet/hull interaction to be carried out within the University Technology Centre at Chalmers, sponsored by Rolls-Royce. The objective of this project was twofold:

1. To gain further insight into the physics behind the waterjet/hull interaction. In particular the negative thrust deduction should be investigated. Why does it occur, and under which circumstances?
2. To develop a rapid, yet reasonably accurate method for estimating the gross thrust of a waterjet driven hull.

Since the investigations of item 1 required a fast and reasonably accurate method for computing the flow, forces and moments of a waterjet driven hull, the method of item 2 had to be developed first. In the following this method will be named the "Pressure Jump Method". This will be described in Chapter 4, while the investigation of the physics behind the thrust deduction will be reported in Chapter 5. First a short introduction the waterjet theory will be given in Chapter 3.

16

3 General Definitions

In this section general definitions, which are frequently used in waterjet system analysis, are introduced. Most of the definitions and formulations in this chapter are taken from reports of the ITTC Specialist Committee on Waterjets [20], [22], [28], [35] and [10].

3.1 Momentum Flux

The waterjet propulsion concept is based on the thrust force gained from the momentum flux change through the system. Low speed velocity enters the system through the capture area. Inside the ducting channel the pump adds momentum to the entrained water and, thereafter, a high-speed jet is spewed out through the nozzle. Writing the momentum flux balance for a control volume gives the resultant force acting on this control volume. In general, momentum flux vector, M, in i direction over a control volume is defined as Equation (3-1).

$$\overline{M}_i = \iint_A \rho u_i (u_k n_k) dA$$

(3-1)

where ρ is the density of the fluid, u is the velocity vector and n is the unit vector normal to the control volume surface.

3.2 Surfaces and Control Volume

Figure 3.1 shows the cross section of a waterjet propulsion unit and the control volume, which is normally applied for the system analysis. The numbering of the surfaces shown in Figure 3.1 is the same as those introduced by van Terwisga [10].
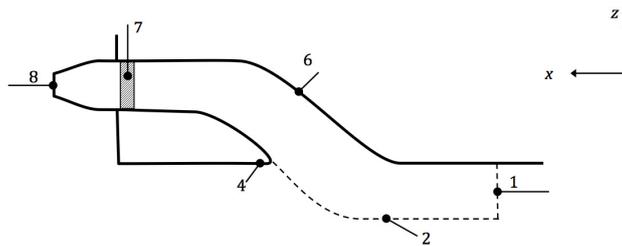
Figure 3.1 Section cut through the waterjet ducting system

Surface 1 is named capture area and is positioned one impeller diameter ahead of the intake ramp tangency point. Avoiding the major flow distortions caused by the intake geometry is the reason for selecting the position of the capture area [28]. Surface 2 in Figure 3.1 shows the dividing streamtube. This streamtube is an imaginary surface, which separates the flow drawn into the ducting system from the

17

rest of the flow field. According to the definition of streamtube, no flow crosses this surface. Surface 4 is the outer-lip surface and surface 6 shows the waterjet system internal material boundaries. Surface 7 is the boundary area of the pump control volume and surface 8 represents the nozzle discharge area.

3.3   Thrust and Thrust Deduction

Having defined the control volume, and considering the coordinate system, x, y, z, to be Cartesian and earth fixed, the thrust force exerted on the control volume may be obtained by applying the momentum conservation law over that control volume. The change in momentum flux over a certain control volume is equal to the sum of the forces acting on that control volume.

$$\iint_{A_1+A_8} \rho u_i(u_k n_k)dA = \iint_{A_1+A_2+A_6+A_8} \sigma_{ij}n_j dA + \iiint_{V_7} \rho F_{pi}dV + \iiint_{V} \rho F_i dV \qquad (\,3\text{-}2\,)$$

where,

$\iint_{A_1+A_8} \rho u_i(u_k n_k)dA$: net momentum flux through control volume

$\iint_{A_1+A_2+A_6+A_8} \sigma_{ij}n_j dA$: external force acting on surface of control volume

$\iiint_{V_7} \rho F_{pi}dV$: body force on control volume

$\iiint_{V} \rho F_i dV$: pump force acting on fluid

The normal vector n points out of the control volume; hence when the velocity vector, u, exits the control volume the product of $u \cdot n$ is positive and when the velocity vector is entering the control volume this product becomes negative.

σ_{ij} is the tensor showing the external forces acting on the control volume. This tensor can be split into two parts as shown in Equation (3-3).

$$\sigma_{ij} = -p\delta_{ij} + \tau_{ij} \qquad (\,3\text{-}3\,)$$

where p is the time averaged pressure and τ_{ij} is the shear stress tensor. δ_{ij} is the Kronecker delta defined as follows:

$$\delta_{ij} = \begin{cases} 1 & if \quad i = j \\ 0 & if \quad i \neq j \end{cases} \qquad (\,3\text{-}4\,)$$

18

The gross thrust, $\vec{T}_g$, is defined as "the force vector pertinent to the change in momentum flux over the selected control volume, acting on its environment" [10]. This is basically the definition of the first term on the left hand side of Equation (3-2). The gross thrust is a force vector but since the horizontal component of this vector is more important, shortly, this component of the gross thrust, $T_{g,x}$, is called the gross thrust, T_g (Equation (3-5)).

$$T_g = - \iint\limits_{A_1+A_8} \rho u_x (u_k n_k) dA$$

(3-5)

Since the gross thrust is the reaction force exerted by the control volume on its environment, the minus sign in the term to the right makes the gross thrust point in the same direction as the net thrust.

Considering the material boundaries of the waterjet system, another thrust force may be defined. "The net thrust, $\vec{T}_{net}$, is defined as the force vector acting upon the material boundaries of the waterjet system, directly passing the force through to the hull" [10]. From now on, the horizontal component of the net thrust vector is going to be called the net thrust, T_{net}, which is defined as Equation (3-6).

$$T_{net} = - \iint\limits_{A_4+A_6} \sigma_x dA - \iiint\limits_{V_7} \rho F_{px} dV$$

(3-6)

Since the surface normal vectors of the control volume point out of the flow control volume, there is a need to use minus signs for the terms on the right hand side.

Employing the definitions for the net thrust and gross thrust, the x-component of Equation (3-2) may be rewritten as follows:

$$-T_g = -T_{net} + \iint\limits_{A_1+A_2+A_8} \sigma_x dA - \iint\limits_{A_4} \sigma_x dA$$

(3-7)

In order to relate the net thrust to the gross thrust, a thrust deduction fraction is defined as Equation (3-8).

$$T_{net} = T_g \left(1 - t_j\right)$$

(3-8)

By applying the definitions of the net thrust and gross thrust, t_j the equation reads as follows:

$$t_j = -\frac{1}{T_g}\left[\iint\limits_{A_1+A_2+A_8} \sigma_x dA - \iint\limits_{A_4} \sigma_x dA\right]$$ (3-9)

Positive thrust deduction fraction means that the net thrust is smaller than the gross thrust and vice versa. It will be discussed in detail in Chapter 5.

It should be noted that the thrust deduction fraction introduced, t_j, is not the same as the conventional thrust deduction fraction, t, employed in the propeller/hull interaction theory. For a conventional propeller, t relates the resistance of the bare hull to the net thrust required for driving the hull at a certain Froude number; but since due to technical issues, it is not easy to measure the net thrust of the waterjet system, the gross thrust is normally employed in the definition of the thrust deduction fraction, t (Equation (3-10)).

$$T_g(1 - t) = R_{bh}$$ (3-10)

where R_{bh} is the bare hull resistance.

The total thrust deduction fraction contains both the jet system thrust deduction, t_j and the thrust deduction fraction, t_r defined by the hull resistance increment, r. The latter thrust deduction is the one normally employed in conventional propeller/hull theory and is defined as follows:

$$T_{net}(1 - t_r) = R_{bh}$$ (3-11)

where,

$$1 - t_r = \frac{1}{1 + r}$$ (3-12)

The combination of Equations (3-8) and (3-11) gives the following equation:

$$T_g(1 - t_j)(1 - t_r) = R_{bh}$$ (3-13)

By neglecting the second order term in Equation (3-13) and comparing it with Equation (3-10), the total thrust deduction, t, becomes equal to the sum of the thrust deduction due to the resistance increment, t_r, and the jet system thrust deduction t_j (Equation (3-14)).

$$t = t_r + t_j$$ (3-14)

After deriving the equations for the net and gross thrust and the thrust deduction, it should be mentioned that obtaining the stress tensor on the capture area and the

dividing streamtube is not straight forward, especially by means of experimental methods. Numerically, it is possible to detect the surface of the streamtube and capture area to extract the forces exerted on them, something that has been accomplished by Bulten [9] and Jiang-Ming [34]. Bulten [9] concluded that the momentum balance for the streamtube control volume was incorrect but van Terwisga [10] mentioned that for higher ship speeds, the momentum flux change through the waterjet system might be a good measure for the resistance increment of the hull since t_j is normally much smaller than t_r.

3.3.1 Capture Area

Water enters the ducting system through area 1, which is called the capture area. Sometimes, it becomes cumbersome to obtain the exact shape of the capture area and, therefore, there are some assumptions for simplifying the shape. Two of the most conventional assumptions for the shape of the capture area are a rectangular or half-elliptical shape which, according to the ITTC Waterjet Specialist Committee should be placed one impeller diameter ahead of the intake tangency point [22], [36]. Kruppa et al. [20], van Terwisga [1996a] and Scherer et al. [2001] observed that in the range of intermediate to high Froude numbers, the width of the capture area is almost constant; hence, in order to reduce the number of variants, the width of the capture area, w_{capt}, is considered to be a constant value which is a function of intake geometry width, w. Empirical widths of the rectangular and half-elliptical capture areas are shown in Figure 3.2. Height of the capture area, h, is varying based on the flow rate through the system and it is a bit higher in half-elliptical intake geometry compared to the rectangular one.
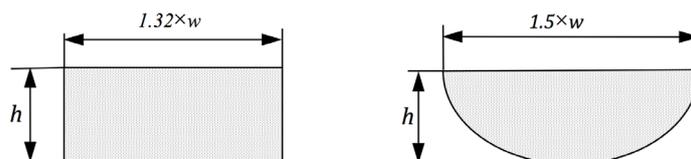
Figure 3.2 Two different assumptions for the capture area geometry [22]

The geometry of the rectangular or elliptical capture area may be defined by the following function [10].

$$\left(\frac{z}{h}\right)^r + \left(\frac{y}{\frac{1}{2}w_{capt}}\right)^r = 1 \qquad (\,3\text{-}15\,)$$

where r defines the shape of the capture area. For $r=2$ it becomes a function which defines a semi-ellipsoid and for $r>100$, it practically defines a rectangle. Different curves obtained from the variation of r are plotted in Figure 3.3.
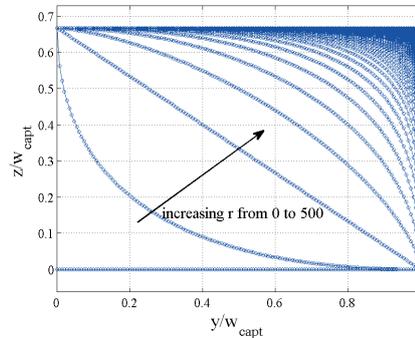
Figure 3.3 Effect of *r* on the curve representing the capture area

In contrast to the findings showing the validity of choosing simple intake geometry, Roberts and Walker [16], using a rectangular capture area, measured the gross thrust as being 10% lower than the thrust obtained using the shape of the actual capture area. Finding out the exact shape of the capture area might be tricky in experiments; however, by employing CFD there are methods to calculate the exact shape. Backward tracing of the streamlines from the impeller surface is one alternative way (Figure 3.4). Another method based on concentration scalar divides the computational field into two different parts. One part is the flow, which passes through the impeller section, while the other represents the rest of the flow; the surface separating these zones defines the boundaries of the intake streamtube and is captured through a post-processing procedure when the flow field solution is converged ([9], [34]).
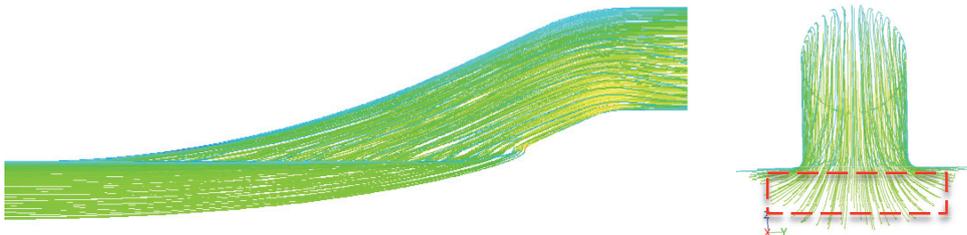
Figure 3.4 Backward tracing of the streamlines for obtaining the capture area; left: side view and right: stern view. The dashed line shows the rectangular capture area.

3.3.2   Jet Flow

In this section, the jet profile and the axial velocity distribution across the nozzle discharge are going to be discussed. Although, after the impeller, there exists a stator inside the nozzle chamber to remove the swirl of the jet, some tangential component of the velocity is still detected in the discharged jet. Moreover, the effect of employing the bulk average velocity for obtaining the jet momentum flux instead

22

of momentum velocity is addressed in this section. Besides, there will be some discussion on the position of vena-contracta of the jet.

3.3.2.1   Swirling Jet Flow

Measurements of the axial velocity of swirling jets show that there are retarded flow regions both in the centreline and close to the outer surface of the jet. The axial flow is well described by Equation (3-16) [20].

$$\frac{u_{8,x}}{u_{8,x\,max}} = \left\{ 1 - \left(\frac{r}{R}\right)^{n} - k\left[1 - \left(\frac{r}{R}\right)^{\frac{3}{2}}\right]^{12} \right\} \qquad (\,3\text{-}16\,)$$

where r is the jet radius; R shows the maximum jet radius. n and k are constants which determine the quantity of retarded flow close to the swirling jet outer surface and centreline of it, respectively. The effect of different n and k can be seen in Figure 3.5. When n goes to infinity, the axial velocity profile becomes more flat at regions close to the outer surface. k values close to zero have the same effect on the jet velocity close to the centreline.
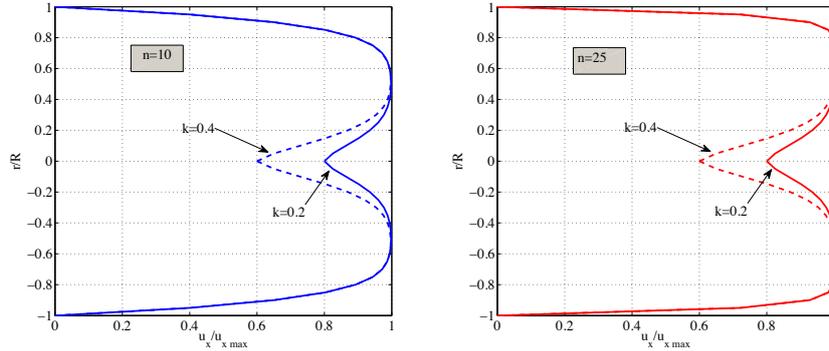
Figure 3.5 Typical axial velocity profile of a swirling jet for different values of n and k.

A sensitivity analysis [20] shows that a moderate rotation has minor effects on the power prediction of the jet system. The slight change in the momentum flux is because of the change in the static pressure of the jet due to the swirl. This reduced static pressure has detrimental effects on the change of momentum flux through the pressure term $\int_{A8}(p_8 - p_0)\,dA_8$ in the momentum equation. The pressure reduction due to swirl, Δp_{swirl}, may be obtained from Equation (3-17) [20].

$$\Delta p_{swirl} = -\rho \cdot \int_{0}^{R} \frac{u_{8\phi}^{2}}{r}\,dr \qquad (\,3\text{-}17\,)$$

where $u_{7\phi}$ is the tangential velocity of the jet. r is the radial distance from the jet centre and R is the jet diameter.

23

3.3.2.2   Jet Momentum Flux Correction

According to the previous section, the axial velocity of the jet flow at the nozzle discharge is non-uniform. Hence, using the average axial velocity for obtaining the jet axial momentum flux causes some error, which should be corrected by introducing a dimensionless momentum flux correction factor, β where $\beta \geq 1$ [37].

This factor accounts for the variation of $u_{8,x}^2$ across the nozzle discharge. β times the momentum flux based on the average axial velocity of the jet is equal to the flux obtained by computing the exact momentum flux (Equation (3-18)).

$$\rho \int u_{8,x}^2 \, dA = \beta \dot{m} \bar{u}_{8,x} = \beta \rho A_8 \bar{u}_{8,x}^2$$

(3-18)

or

$$\beta = \frac{1}{A_8} \int \left(\frac{u_{8,x}}{\bar{u}_{8,x}} \right)^2 dA$$

(3-19)

Modelling the entire impeller geometry, Hu and Zangeneh [21] calculated the velocity distribution at the nozzle outlet and compared its bulk average to the actual momentum velocity to obtain β. They reported a momentum flux correction factor of β=1.000386 which means that there will be an error of approximately 0.4% in case the bulk average is employed for the momentum flux calculation instead of the momentum velocity.

3.3.2.3   Vena-Contracta

The vena-contracta of an incompressible jet flow represents the section of the jet in which the average static pressure is identical to the ambient pressure. Depending on nozzle design, vena-contracta may occur at the nozzle discharge section or further downstream. Basically, the flow leaves the nozzle tangentially. As soon as the jet exits the nozzle, the pressure on the outer surface of the jet becomes atmospheric. Depending on the curvature of the nozzle exit, there might be a pressure gradient on the exit part of the nozzle. Employing a RANS solver (FLUENT), the flow through two nozzles with different exit designs is studied. The flow is assumed to be laminar and axisymmetric. Figure 3.6 shows the jet profile of two possible nozzle designs, one with the contraction and another with the horizontal exit. The jet leaves the nozzle tangentially to the exit. By tracing the streamlines, the tangency of the flow to the nozzle exit is shown in Figure 3.7. The location of the vena-contracta is shown for the nozzle with the contraction. The pressure distribution inside the nozzle is also shown in Figure 3.7. The jet continues contracting until the average pressure at the vertical section of the jet reaches atmospheric pressure. From this section on, the jet continues without any contraction. One may conclude that for

24

nozzle designs without exit contraction, there will not be a vena-contracta and it is a fair approximation to assume that the average pressure at the nozzle exit will be atmospheric. According to the proposed method by 25th ITTC [35], for nozzle designs with the vena-contracta, momentum flux may be measured at the nozzle discharge where its diameter may be accurately measured. Then, bollard pull calibration procedure can be applied to cancel the possible errors due to this assumption. This calibration yields a relationship between the flow rate and jet thrust.
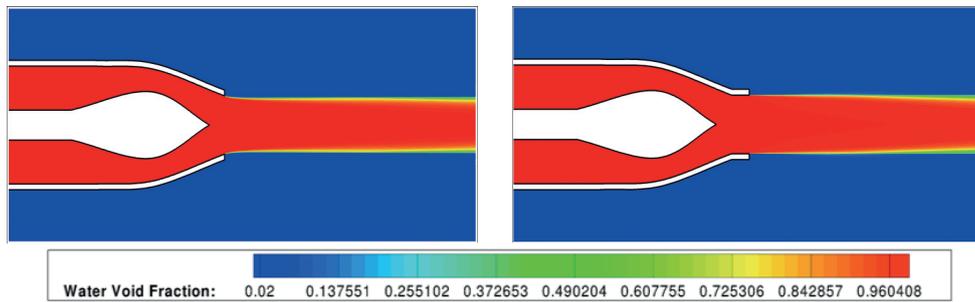

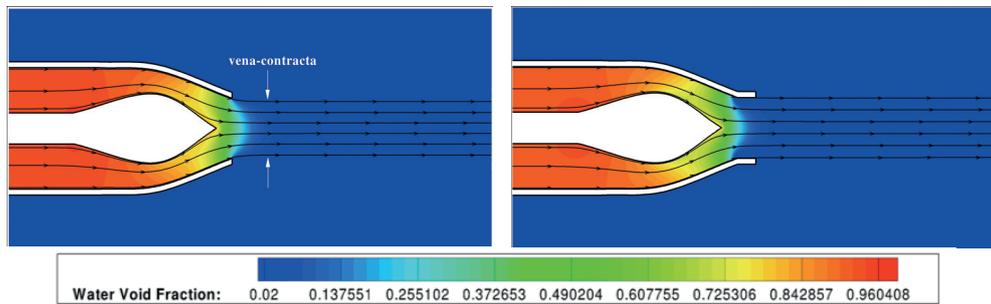Figure 3.6 Water void fraction of the flow through nozzles exit with and without contraction

Figure 3.7 Pressure distribution inside nozzles with and without contraction

4 Pressure Jump Method

Generally, the duty of a centrifugal pump is to increase the head of the flow. The rise of the flow head, which occurs by passing through the impeller, might be interpreted as an abrupt pressure rise at the section of impeller, which is generally called pressure jump. The occurred pressure jump is the fundamental theory behind the developed method for modelling the waterjet propulsion system and, therefore, this approach is called the Pressure Jump Method. The following sections describe the theory behind this method, its mathematical formulation and combination with a potential flow solver.

4.1 Formulation

To start with, the force balance for the waterjet-hull system must be formulated. The contribution of different parts of the system on the total resistance is depicted in Figure 4.1. In this figure, R_H is the hull resistance, R_D is the ducting channel drag and R_N is the drag force of the nozzle chamber. F_p is the force exerted by the impeller.
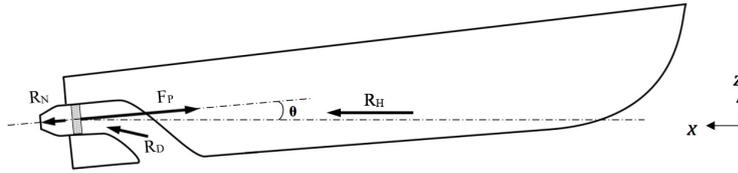
Figure 4.1 Force balance of the waterjet-hull system

Writing the force balance in the x-direction for the shown system, Figure 4.1, results in Equation (4-1).

$$F_{P,x} = R_H + R_{D,x} + R_{N,x}$$

(4-1)

Because of the action of the pump, there is a difference in pressure between the sides of the impeller. In fact, this pressure jump at the impeller section is the main source of the created thrust force of the waterjet system. A simplified sketch of the nozzle geometry is shown in Figure 4.2. Assuming a constant pressure on each side of the impeller disk and considering the fact that the impeller thrust force, F_p, is transmitted through its shaft which has an angle of θ with the horizontal plane, the equation for balancing the force in the x-direction reads:

$$F_{P,x} = \left(P_{after} - P_{front}\right)A_{impeller} \cdot \cos\theta$$
$$= \Delta p \cdot A_{impeller} \cdot \cos\theta \qquad\qquad (4\text{-}2)$$

where P_{front} and P_{after} are the pressures just before and after the impeller disk, respectively, and Δp shows the difference between these two. $A_{impeller}$ is the area of the impeller disk.
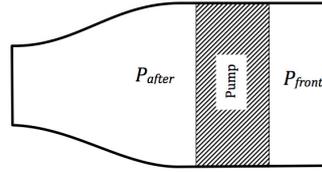
Figure 4.2 Schematic presentation of the nozzle section

Moreover, it is possible to denote the nozzle resistance, $R_{N,x}$, in the following integral form:

$$R_{N,x} = \iint\limits_{S_{nozzle}} \sigma.n_x ds \qquad\qquad (4\text{-}3)$$

where σ is the mean stress, S_{nozzle} is the internal surface of the nozzle chamber and n_x is the normal unit vector in x-direction.

One can split the stress tensor shown in Equation (4-3) into normal and shear stress:

$$\iint\limits_{S_{nozzle}} \sigma.n_x ds = \iint\limits_{S_{nozzle}} p.n_x ds + \iint\limits_{S_{nozzle}} \tau.n_x ds \qquad\qquad (4\text{-}4)$$

where p is the pressure and τ shows the shear stress tensor.

The actual flow inside the nozzle chamber may be considered as the superposition of two different cases. The first case is the flow through the nozzle chamber without any pressure jump but with the same flow rate as in reality. Adding a constant pressure rise to the first case results in the actual flow. According to the Navier-Stokes equations, in an incompressible flow, it is the pressure gradient which is important in defining the flow field and not the absolute pressure; hence, by subtracting the pressure jump, which is a constant amount inside the nozzle chamber, the velocity field inside the nozzle still remains the same as in reality.

Following this assumption, the pressure, p, The pressure after the impeller disk may be split into the static pressure inside the nozzle in the absence of the pump system, p_{WOP}, plus a constant pressure jump, Δp, occurring due to the action of the pump; thereby, one may rewrite the second term in Equation (4-4) as Equation (4-5).

$$\iint_{S_{nozzle}} p \cdot n_x ds = \iint_{S_{nozzle}} p_{WOP} \cdot n_x ds + \iint_{S_{nozzle}} \Delta p \cdot n_x ds \qquad (\,4\text{-}5\,)$$

Since the velocity field inside the nozzle chamber does not change with the constant pressure jump, the shear stress tensor, τ, will remain the same in both cases.
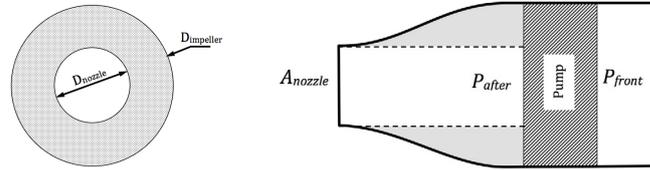
Figure 4.3 Schematic presentation of the nozzle section

The second term of Equation (4-5) can be simplified into Equation (4-6). As mentioned earlier, this term shows a constant pressure increase inside the nozzle chamber. Since Δp is constant, it can be moved out of the surface integral in Equation (4-5). The remaining term inside the integral is simply the projected area of the nozzle in the x-direction. This area is shown in grey in Figure 4.3.

$$\iint_{S_{nozzle}} \Delta p \cdot n_x ds = \Delta p \big(A_{Impeller} - A_{nozzle} \big) \cdot \cos\theta \qquad (\,4\text{-}6\,)$$

where $A_{impeller}$ and A_{nozzle} consequently make up the impeller disk and nozzle discharge areas.

By introducing Equation (4-6) into Equation (4-5) and then inserting the resultant equation into Equation (4-3), a new expression for the resistance of the nozzle, $R_{N,x}$, is derived. By inserting this equation and Equation (4-2) into the original force balance equation (Equation (4-1)), the following equation emerges:

$$\Delta p \cdot A_{impeller} \cdot \cos\theta = R_H + R_{D,x}$$
$$+ \left[\Delta p \big(A_{impeller} - A_{nozzle} \big) \cdot \cos\theta + \iint_{S_{nozzle}} p_{WOP} \cdot n_x ds + \iint_{S_{nozzle}} \tau . n_x ds \right] \qquad (\,4\text{-}7\,)$$

Simplifying this equation gives the following:

$$\Delta p \cdot A_{nozzle} \cdot \cos\theta = R_H + R_{D,x} + \left[\iint\limits_{S_{nozzle}} p_{WOP} \cdot n_x \, ds + \iint\limits_{S_{nozzle}} \tau . n_x \, ds \right] \qquad (\text{4-8})$$

The right hand side of Equation (4-8) is equal to the total resistance of the entire system without pressure jump and is named R_{TWOP}.

$$R_{TWOP} = R_H + R_{D,x} + \left[\iint\limits_{A_{nozzle}} p_{WOP} \cdot n_x \, ds + \iint\limits_{A_{nozzle}} \tau . n_x \, ds \right] \qquad (\text{4-9})$$

By introducing Equation (4-9) into Equation (4-8) the equation for obtaining the required pressure jump to balance the resistance forces reads,

$$\Delta p = \frac{R_{TWOP}}{A_{nozzle} \cdot \cos\theta}. \qquad (\text{4-10})$$

4.2   Potential Flow Assumption

The following assumes that the flow from the capture area to the nozzle exit is inviscid and, therefore, there is no head loss inside the ducting channel. In other words, the total head at section 8 becomes equal to the total head at section 1 plus the constant pressure jump, Δp. This is expressed through Bernoulli's equation in Equation (4-11). The pressure at the nozzle outlet section is assumed to be atmospheric. Subscripts applied in Equation (4-11) are based on the notation presented in Figure 3.1;

$$\left[\bar{p}_1 + \rho g \bar{h}_1 + \frac{1}{2}\rho \overline{u_1^2} \right] + \Delta p = \bar{p}_{atm} + \rho g \bar{h}_8 + \frac{1}{2}\rho \overline{u_8^2} \qquad (\text{4-11})$$

where ρ is the water density and g is the gravitational acceleration. $\bar{p}_1$ and $\bar{p}_{atm}$ represent the average pressures at the capture area and atmospheric pressure, respectively. The average height of the capture area and nozzle outlet section are denoted by $\bar{h}_1$ and $\bar{h}_8$, respectively. $\bar{u}$ and $\bar{u}_8$ represent the average velocities at sections 1 and 8.

All terms in Equation (4-11) are known except the term containing the jet velocity, $\bar{u}_8$. By rearranging the equation for obtaining $\bar{u}_8$ and then dividing both sides by the undisturbed velocity, u_∞, the following equation emerges.

$$\frac{\bar{u}_8}{u_\infty} = \pm \sqrt{\frac{(\bar{p}_1 - \bar{p}_{atm})}{\frac{1}{2}\rho u_\infty^2} + \frac{\Delta p}{\frac{1}{2}\rho u_\infty^2} + \frac{2g(\bar{h}_1 - \bar{h}_8)}{u_\infty^2} + \frac{\overline{u_1^2}}{u_\infty^2}}$$ (4-12)

or alternatively,

$$\frac{\bar{u}_8}{u_\infty} = \pm \sqrt{\overline{C_p}_1 + \Delta C_p + \frac{2}{Fn^2} \cdot \frac{(\bar{h}_1 - \bar{h}_8)}{L_{pp}} + \frac{\overline{u_1^2}}{u_\infty^2}}$$ (4-13)

where L_{pp} is the length between perpendiculars and Fn is the Froude number of the craft.

$$Fn = \frac{u_\infty}{\sqrt{g \cdot L_{pp}}}$$ (4-14)

In the literature $\frac{\bar{u}_8}{u_\infty}$ is called the Nozzle Velocity Ratio, NVR, but since in the pressure jump method it is assumed that the pressure at the nozzle discharge section is atmospheric this velocity ratio can be called Jet velocity ratio, JVR, as well. According to the discussion in Section (3.3.2), if the nozzle discharge geometry is parallel NVR and JVR have the same value; but if the nozzle contracts at the jet discharge section, there will be an error in calculation of NVR, which can be solved by calculating the vena-contracta of the jet.

30

4.3 Numerical Simulation

The potential flow is computed using SHIPFLOW [38], a suite of computer codes based on in-house research. The XPAN module is a potential flow panel method, using Rankine sources on the hull and part of the free surface. A Neumann boundary condition for the potential is applied on the hull (corresponding to zero normal velocity) and a combined kinematic and dynamic condition is applied on the free surface at its exact location. The latter is obtained iteratively.

In the present study, the panels are extended into the duct all the way to the nozzle exit, where a velocity u_8 in the direction of the nozzle axis is specified. This is achieved by covering the exit plane with panels with the normal velocity u_8 at their control points. Figure 4.4 shows the upper part of the computational domain, the water below the free surface and outside the hull, as well as the duct back to the exit. The outer domain boundary is assumed to lie at an infinite distance. A potential flow solution can, thus, be obtained not only around the hull, but also inside the duct, with the given exit velocity, u_8. Note that the free jet is outside of the computational domain. In principle, this has no effect on the solution, but in practice, it makes it difficult for the free surface panels in the wake to satisfy the boundary condition; consequently, if the exit is close, instabilities may occur. So far, this has been resolved by moving the jet exit slightly forward.
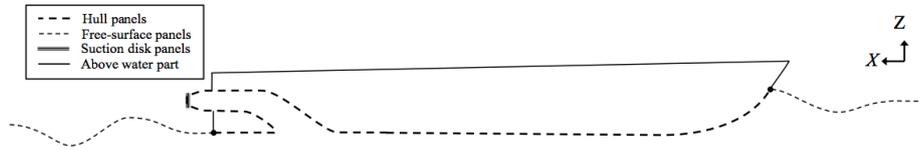
Figure 4.4 The computational domain is located below the dashed line, representing panelized surfaces.

The potential flow solution contains the pressure distribution around the hull and in the duct for the given u_8. This yields the wave resistance of the hull and an approximate pressure resistance of the duct. The latter is approximate, since SHIPFLOW assumes a constant total head in the entire computational domain, while in the duct the total head is in reality somewhat reduced, as discussed above. Since both the velocity (specified by u_8) and the height of the nozzle are correct, the pressure inside the duct will be over predicted which may result in some computational error.

The frictional resistance of the hull is computed by the boundary layer module XBOUND in SHIPFLOW based on the computed pressure. There is no need to include the RANS module for hulls like the ITTC proposed hull [22], with a wide submerged transom, in which the boundary layer stays relatively thin over the entire

31

hull. Inside the duct, the friction coefficient is approximately computed by extrapolating it from the hull. As long as the wetted surface is correct, this is a minor approximation.

Note that no pump force is used in the SHIPFLOW solution. The key is to adjust the exit velocity u_8 such that Equations (4-10) and (4-13) are satisfied simultaneously. This has to be done iteratively. After each iteration, all terms on the right hand side of Equation (4-9) are known, which means that R_{TWOP} can be computed and inserted into Equation (4-10) to obtain Δp. This is then inserted (non-dimensionalized) into Equation (4-13), where C_{p1} is obtained as the potential flow pressure on the hull at point A and u_1^2 is taken as the average of the squared velocity at the capture area, considering the boundary layer velocity profile computed by XBOUND. A new u_8 can then be obtained and the process repeated. It is convenient to start the process by neglecting the resistance of the duct.

To account for the trimming moment due to the water jet, the position (height) of the thrust force $\Delta p \cdot A_{nozzle}$ is specified at the centre of the impeller disk along the shaft line. SHIPFLOW then automatically trims the hull to balance the moment created by the total resistance force and the thrust.

4.3.1 Test Case

The hull investigated in this study is R/V ATHENA, the hull selected by the ITTC Specialist Committee on Waterjets [22]. This Committee was composed of several Institutes that conducted some resistance and self-propulsion tests on ATHENA. Being a high-speed generic hull with a wide transom stern, having a substantial database of resistance, powering and flow information this hull satisfied several criteria taken into account by the Committee in choosing the proper hull. Some fundamental data are provided in Table 4.1. Moreover, Figure 4.5 depicts the body plan of the hull.

Table 4.1 Fundamental data for ATHENA [22]

Length	50.29 m
Maximum beam	6.68 m
LOW	46.9 m
Displacement	260 tons
Volume	257.5 m^3
b/B (Transom width ratio)	0.828
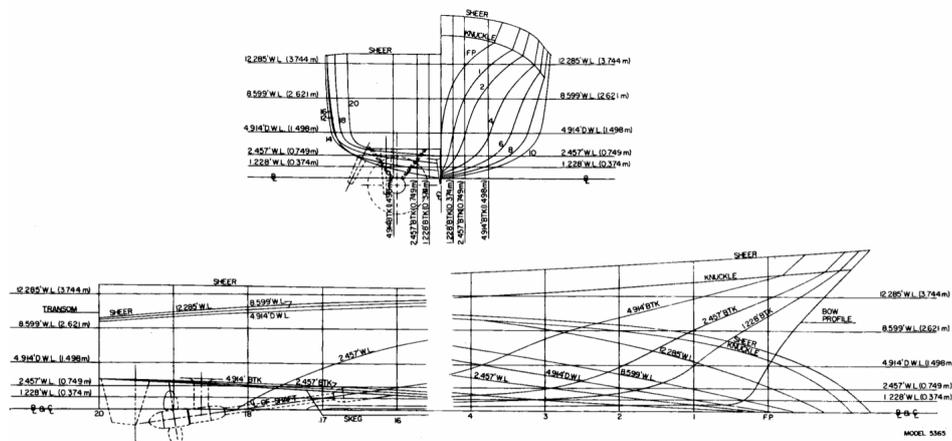
Figure 4.5 Profile lines and body plan for the R/V ATHENA [22]

A pair of axial flow waterjets was fitted into the model with a scale ratio of 8.556. The self-propulsion test set-up and a general view of the jet flow are shown in Figure 4.6 and Figure 4.7, respectively.

Figure 4.6 Model scale self-propulsion test setup [39]

Figure 4.7 Model scale ATHENA with working waterjets [40]

There was a lack of agreement among different Institutes involved in the model testing on some issues like the hull displacement and the bare hull resistance test. Due to this controversy, the test displacement varied by 30kg (Figure 4.8). The intention was to perform the bare hull resistance test with the covered intake openings; however, certain Institutes conducted the experiments with open intakes that made the ducting channel fill up with water [40].

Figure 4.8 Model test displacement [40]
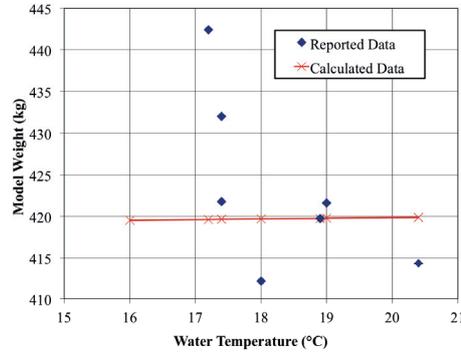
The bare hull resistance, bare hull and working inlet survey, jet velocity profile, momentum flux calculation and the full scale data prediction were investigated through a series of experiments [40], each of which is going to be discussed in the Validation section.

4.3.2   Panelization

In order to be able to create panels on the hull and the ducting channel, the whole system has been divided into multiple body groups and then assembled next to each other. Figure 4.9 depicts the general appearance of the panelization of the whole system. A closer look at the ducting channel panelization and the suction disk positioning is shown in Figure 4.10.
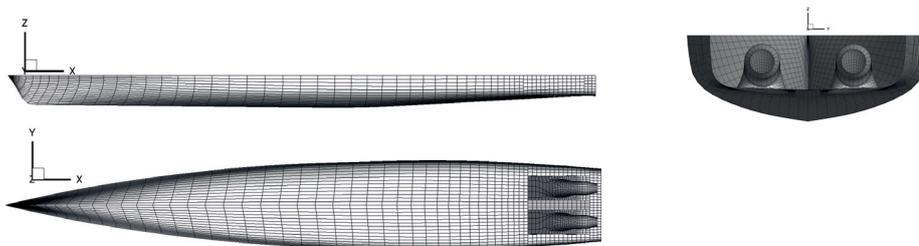
Figure 4.9 Panelization of the hull with intakes

In the original geometry, the nozzle discharge is located outside the hull but as seen in Figure 4.9, the geometry has been modified and the jet discharge section is positioned somewhere before the transom inside the hull. As mentioned, this geometrical modification has been made to avoid the interaction of the suction disk with transom free surface panels. In the original geometry, when the suction disk is closer to the transom free surface, the pronounced source strength distribution on the suction disk and its interaction with the transom free surface panels makes it hard to satisfy the dry transom condition which simply is the tangency of the

34

transom free surface to the transom. Shortening the cylindrical part of the ducting channel is a solution for making the effect of this numerical interaction weaker. It should be noted that the angle of the nozzle discharge relative to the horizontal plane must not change in this geometrical modification.
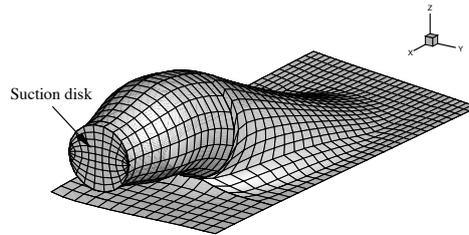
Figure 4.10 Panelization of the intake geometry and the suction disk
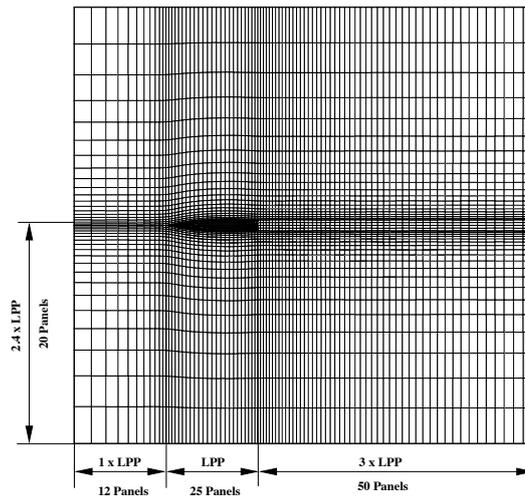
Figure 4.11 Panelization of the free-surface at $Fn = 0.6$

The computational domain size and free surface panelization for $Fn = 0.6$ are shown in Figure 4.11. The sufficient number of free surface panels along the hull is 20-30 panels per characteristic wavelength, n_λ [38]. This number is obtained by the following equation:

$$n_\lambda = \frac{1}{2\pi Fn^2} \qquad (\,4\text{-}15\,)$$

As mentioned earlier, there is a strong interaction between the suction disk and the free surface panels at the transom, causing a problem to satisfy the dry transom criteria. As indicated before, this problem was partially solved by shortening the

35

duct channel exit part. Moreover, coarser panels for the free surface at the transom must be used. Since the suction velocity applied on the disk varies with Froude number, the size of the first free-surface panel at the transom also varies.

4.3.3 Rope Force

Since the Reynolds number for model scale and full scale differs, the frictional resistance coefficient will also vary. In order to compensate for the deficit of the friction coefficient at full scale, an extra tow force is applied to the model in the self-propulsion test to unload the propulsor so that this propulsor only needs to overcome the full-scale frictional resistance. This extra force is called 'Rope Force' or 'Correction Allowance'.
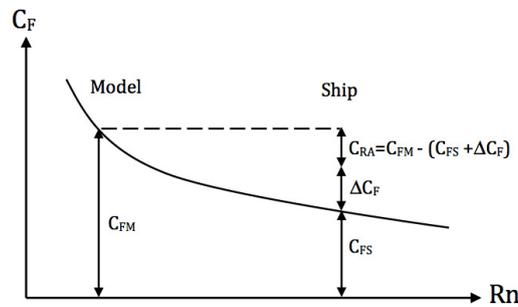
Figure 4.12 Illustration of the model-ship frictional resistance and the roughness allowance correlation

Figure 4.12 illustrates the friction coefficient variation from the model scale, C_{FM}, to the full scale, C_{FS}. The size of these coefficients can be obtained from the ITTC-57 proposed formula (Equation (4-16)) or other methods:

$$C_F = \frac{0.075}{(\log_{10} Rn - 2)^2} \qquad (\text{4-16})$$

The total friction resistance coefficient of the full scale hull is equal to the friction coefficient at the full scale obtained from Equation (4-16) plus the roughness allowance, ΔC_F. Roughness allowance is an empirical surface roughness correction applied because of the larger surface roughness of the ship compared to the smooth surface of the model and is set to $\Delta C_F = 0.4 \times 10^{-3}$.

The non-dimensional rope force coefficient is expressed as Equation (4-17):

$$C_{RA} = C_{FM} - (C_{FS} + \Delta C_F) \qquad (\text{4-17})$$

Finally, the dimensional form of the rope force, which should be applied to the model, is obtained as follows:

$$R_A = \frac{1}{2}\rho_M U_M^2 S_M C_{RA}$$

where ρ_M is the water density of the model test, U_M is the model speed and S_M is the wetted surface area of the model.

4.3.4   Wave Making Resistance Correction

As mentioned earlier, in this study, the potential flow solver is employed to model the flow around the hull. This assumption results is an over prediction or under prediction of the hull resistance in different Froude number ranges. In the potential flow solver employed, XPAN, a dry transom condition is applied for all flow regimes, which means that the flow at the transom leaves the hull tangential to it (Figure 4.13). Although this is a reasonable assumption for the intermediate and higher Froude numbers, $Fn > 0.4$, for the lower Froude numbers, the transom is wetted and the dry transom condition is no longer valid. Whenever the transom is wet, a higher hydrostatic pressure is exerted on the stern compared to the dry transom, and accordingly, in a lower Froude number, e.g. $Fn = 0.3$, XPAN predicts larger resistance due to the dry transom condition applied. Moreover, at higher Froude numbers, $Fn > 0.6$, some highly non-linear effects in the inviscid flow, including flow spray, breaking or over turning waves, become increasingly important. These effects are not captured in the potential flow solver and, therefore, the resistance of the hull is under predicted in such Froude number ranges.
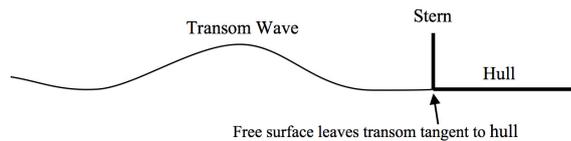
Figure 4.13 Dry transom condition

In order to predict the required powering more accurately, hull resistance must be predicted as precisely as possible. Hence, before employing the calculated hull resistance for balancing the resistance with the thrust of the propulsion system, the predicted resistance by XPAN must be corrected. The correction is accomplished through the formulas introduced by Höglund [41] similar to those suggested by Harris and Schulze [42]. This method assumes that the computed skin friction is close to the values measured and that this correction is only applied to the wave making resistance of the hull obtained from pressure integration and the transverse

wave cut method. The corrected wave-making resistance factor is shown in Equations (4-19):

$$C_{W-corrected} = (1 + K_{CW}) \cdot C_W$$

(4-19)

where C_W is the wave making resistance coefficient obtained from pressure integration on the hull. $C_{W\text{-}corrected}$ is the corrected wave-making resistance coefficient, which is corrected through the K_{CW} correction factor.

Höglund [41] obtained the correction factors based on resistance measurements for the AMECRC systematic series hulls, which are semi-displacement hulls that operate between displacement and planning modes, i.e. $0.3 < Fn < 1.0$. These types of hulls are rather slender and characterized by flared bow sections. The immersed transom becomes dry when speed increases. Moreover, these hulls are known to offer better sea-keeping performance in rough seas than the hard chine planning boats. The AMECRC series consists of 14 models of transom stern, round bilge mono-hulls [41]. Some characteristic data of the model geometries employed in the AMECRC series are shown in Appendix B.

Correction factor K_{CW} employed in Equations (4-19) was supposed to be functions of the hull speed *Fn*, the length-to-beam ratio *L/B*, the beam-to-draft ratio *B/T*, the block coefficient C_b and the hull displacement *Δ* which was used in the non-dimensional form of slenderness coefficient $L/\nabla^{\frac{1}{3}}$. Finally, K_{CW} was defined as Equations (4-20). Non-linear regression was carried out in order to find the constants, $a_1, ..., a_{25}$, with the result shown in Appendix B.

$$
\begin{aligned}
K_{CW} = & \left[a_1 + a_2 \cdot \frac{L}{B} + a_3 \cdot \frac{B}{T} + a_4 \cdot \frac{L}{\nabla^{\frac{1}{3}}} + a_5 \cdot C_b \right] \cdot Fn^0 \\
& + \left[a_6 + a_7 \cdot \frac{L}{B} + a_8 \cdot \frac{B}{T} + a_9 \cdot \frac{L}{\nabla^{\frac{1}{3}}} + a_{10} \cdot C_b \right] \cdot Fn^1 \\
& + \left[a_{11} + a_{12} \cdot \frac{L}{B} + a_{13} \cdot \frac{B}{T} + a_{14} \cdot \frac{L}{\nabla^{\frac{1}{3}}} + a_{15} \cdot C_b \right] \cdot Fn^2 \\
& + \left[a_{16} + a_{17} \cdot \frac{L}{B} + a_{18} \cdot \frac{B}{T} + a_{19} \cdot \frac{L}{\nabla^{\frac{1}{3}}} + a_{20} \cdot C_b \right] \cdot Fn^3 \\
& + \left[a_{21} + a_{22} \cdot \frac{L}{B} + a_{23} \cdot \frac{B}{T} + a_{24} \cdot \frac{L}{\nabla^{\frac{1}{3}}} + a_{25} \cdot C_b \right] \cdot Fn^4
\end{aligned}
$$

(4-20)

4.4   Validation of Pressure Jump Method

4.4.1   Experimental Measurements

The ITTC Specialist Committee on Waterjets [22][28][40], completed an extensive study and a series of measurements on R/V ATHENA in order to investigate the waterjet/hull interaction phenomenon and defined a standard methodology for the performance of waterjet self-propulsion tests [35]. Multiple Institutes were involved in this study and each of them went through a similar procedure to conduct the resistance and self-propulsion tests. Subsequently, each Institute provided a separate data set containing the final measurements requested by the ITTC Specialist Group on Waterjets. Due to the confidentiality of the Institutes in charge of each data set, the measurements of each Institute were marked by a letter instead of the name of the Institute. The resistance test was accomplished for a Froude number in the range of $0.1 < Fn < 0.7$ but the self-propulsion test was carried out for only $Fn = 0.6$.   The size of the towing tanks, in which the measurements were conducted, differed and resulted in 9% discrepancy in the resistance test results. The main source of this discrepancy was the blockage and/or shallow water effect in the smaller towing tanks. Accordingly, the final test results were split into those obtained from small tanks and those from the larger tanks. The data shown in the following bare hull measurements are from the larger towing tanks.

4.4.2   Results

Computational results obtained from the combination of potential flow simulation and the pressure jump method are presented in this section to validate the pressure jump method.

Figure 4.14 shows the predicted wave pattern around the self-propelled hull. The pressure distribution equivalent to the wave pattern shown is plotted in Figure 4.15. During the iterations required to obtain the correct pressure jump, Δp, and corresponding JVR, the pressure at the capture area, $\overline{C_p}_1$ must be recorded and used in the equation for Δp (Equation (4-10)). Figure 4.16 depicts the pressure distribution across the hull at the capture area section. In fact, $\overline{C_p}_1$ is the average of the pressure coefficient curve located inside the dashed rectangle. The pressure at the centre of the capture area is fairly close to the average pressure across the capture area. In practice, $\overline{C_p}_1$ may be replaced by C_{p1} in Equation (4-13).

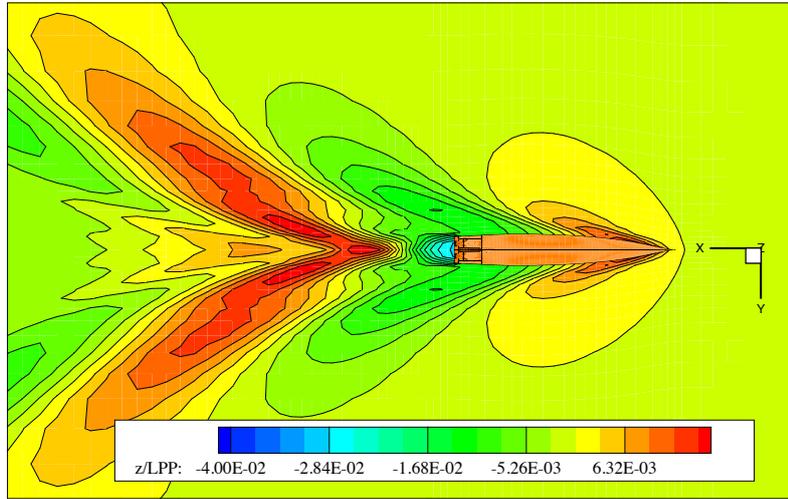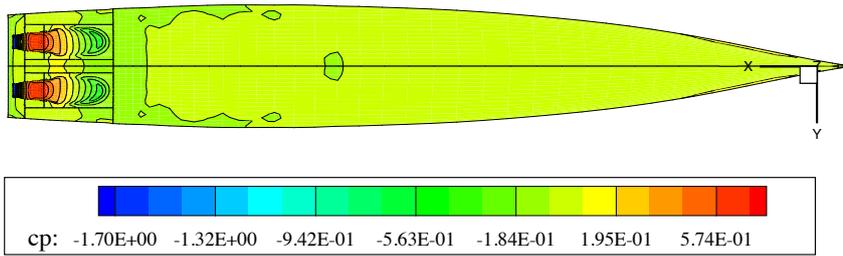Figure 4.14 Computed Wave Pattern around the self-propelled hull at *Fn*=0.6

Figure 4.15 Computed Pressure distribution on the hull and ducting system at *Fn*=0.6
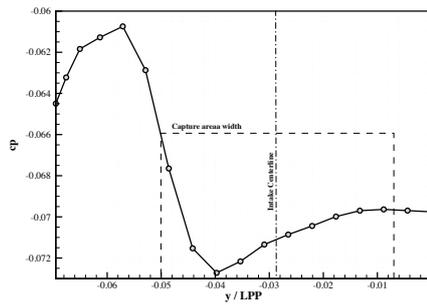
Figure 4.16 Computed Pressure distribution at the capture area section at *Fn*=0.6

A closer look at the pressure distribution inside the ducting channel is shown in Figure 4.17. Since there is no actual pressure jump in the potential flow simulation

inside the ducting channel due to the action of the pump, the pressure at the nozzle discharge is negative, which is not the case in reality. In fact, the pressure jump is exactly large enough to yield zero pressure at the exit.
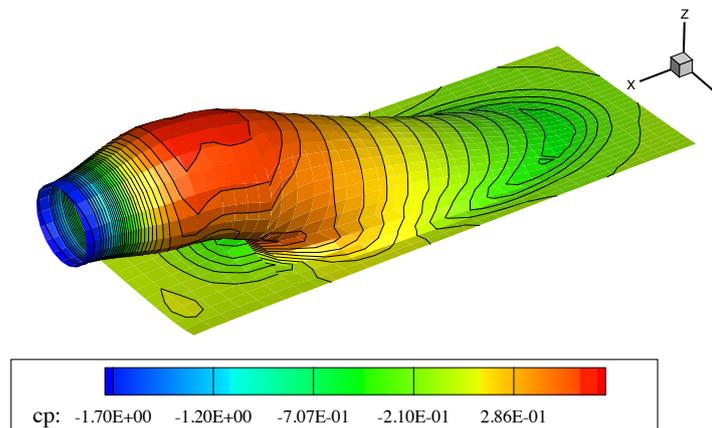
Figure 4.17 Computed Pressure distribution inside the ducting channel at *Fn*=0.6
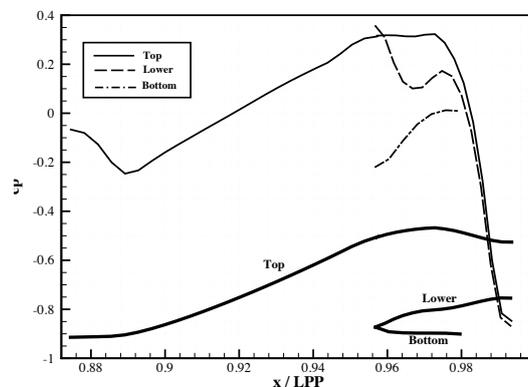
Figure 4.18 Computed Pressure distribution on the ducting channel mid section

Figure 4.18 shows the same information as given in Figure 4.17, but only at the mid-section of the ducting channel. Neglecting the low pressure inside the contracted part of the nozzle, which is not realistic here, the lowest pressure is observed somewhere close to the intake tangency point to the hull, and to some extent, the lower lip part. These are the regions where some cavitating flow may be observed. Moreover, the top part of the ducting channel, where the flow is forced to bend towards horizontal direction, has the highest pressure. These high-pressure and low-pressure zones may create a trimming moment, the direction of which depends not

only on the size of these upward or downward forces, but also on the pivot point position. The pivot point for a hull is its centre of floatation (CoF). This effect will be further discussed in Chapter 5.
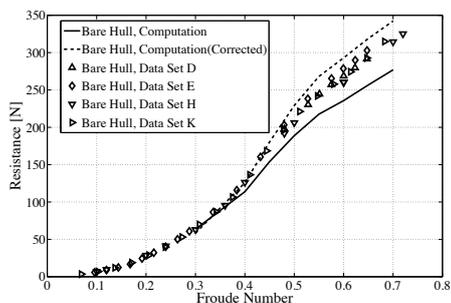
Figure 4.19 Resistance of the bare hull
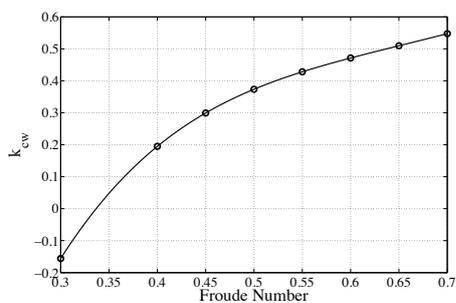
Figure 4.20 Wave making resistance correction factor for R/V ATHENA

Figure 4.19 depicts the predicted bare hull resistance and its comparison with the measurement. The original resistance curve from the potential flow simulation, the solid line, under predicts the actual resistance of the bare hull in the most of the Froude number range. Employing the originally calculated resistance causes some basic error, especially for the self-propelled hull, where the jet system flow rate is a function of the hull resistance. To solve the under prediction resistance problem, the wave making resistance of the hull is corrected based on the proposed method in section 4.3.4. The corrected resistance curve, plotted by the dashed line, shows a better correlation with the measurement. The same correction is applied to the resistance of the hull with intakes, as well. The corrected resistance is used for obtaining the pressure jump in Equation (4-10).

Figure 4.21 Trim angle versus Froude number

Figure 4.21 shows the variation of the trim angle for both the bare hull and the self-propelled hull against the Froude number. Comparing the computed bare hull trim angle with those obtained from the measurement, it is clearly seen that the calculated trim angle is under predicted for Froude numbers larger than 0.45; as the

42

Froude number increases further, the deviation increases. The same method as applied for correcting the resistance of the hull can be used to correct the trim angle as well. But since the original trim angle for the AMECRC systematic series, which were used for obtaining the correction formulas, was not available, no correction was applied to the trim angle.

Comparing the bare hull trim angle with the self-propulsion trim angle, they are the same for Froude numbers below 0.55. For higher Froude num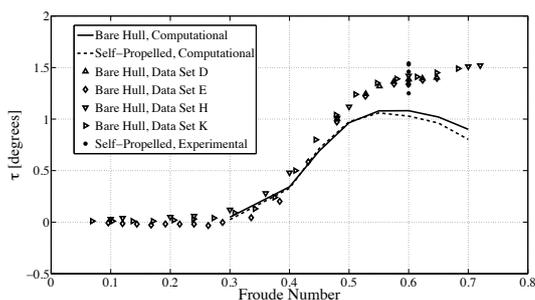bers, the trim angle of the self-propelled hull becomes slightly smaller than the bare hull trim angle. The reasoning behind the lower trim angle of the self-propelled hull must be related to the action of the waterjet system, which causes a bow down trimming moment. Various potential effects, which may contribute to the observed bow down trimming moment, are discussed in Section 5.2.1.
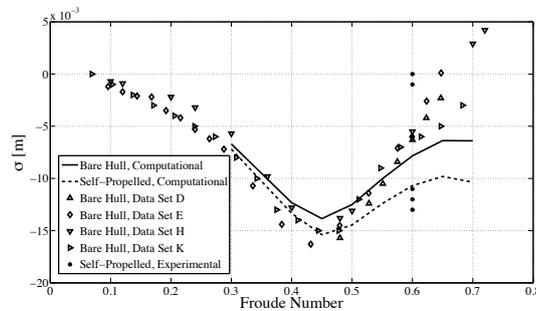
Figure 4.22 Sinkage at $\frac{1}{2}$ LPP versus Froude number

Figure 4.22 depicts the sinkage of the hull measured at half LPP. Since the vertical component of the coordinate system is pointing upwards, the negative values for the sinkage means that the hull actually sinks more deeply. Comparing the bare hull sinkage with the measurement shows a good agreement with Froude numbers below 0.6; but for higher Froude number, computed sinkage under predicts the measurement. Comparing the computed self-propulsion sinkage with the measurement is a bit tricky since the scatter for the measured values is large.

Computed sinkage for the bare and self-propelled hulls demonstrates that the hull with the waterjets sinks more deeply compared to the bare hull. The increased sinkage of the hull in self-propulsion may be analysed in connection with the waterjet induced pressure and possible lift force of the ducting channel. A more detailed discussion on this topic is presented in Section 5.2.1.

An interesting point, which may be noticed from the comparison of Figure 4.21 and Figure 4.22, is the Froude number that causes the bare hull and self-propelled hull sinkage and trim start to deviate from each other. This deviation starts at $Fn = 0.55$ for the trim angle, while the sinkage starts to deviate earlier at $Fn = 0.4$. The

43

indicated fact needs to be investigated further for rendering the effect of sinkage and trim angle on the hull resistance increment.
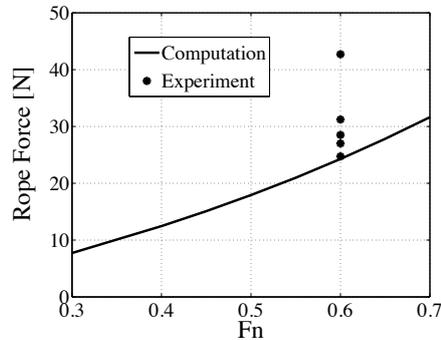
Figure 4.23 Rope force versus Froude number

According to the method proposed in section 4.3.3, an extra tow force is applied to the model in the self-propulsion computation. The purpose of this additional force is to compensate for the increased frictional resistance in the model scale. Figure 4.23 shows the force applied in different Froude numbers. The ITTC-57 friction coefficient formula has been used to calculate the friction coefficients for the model and the ship. Compared to the applied rope forces in the experiment, the employed rope force in the numerical simulation is smaller than most of those used in the experiment. There is a spread of 44.6% for the tow force selected in the experiment. This scatter seems quite large. Different water temperatures and roughness allowances may cause 15% difference in the rope force; however, this cannot explain the spread of the tow forces used.

The computed boundary layer profile at the centreline of the capture area is plotted in Figure 4.24. This figure shows that by increasing the Froude number, the boundary layer profile becomes slightly flatter. This may be in regard to the increasing Reynolds number or possibly according to the variation of the intake velocity.

Figure 4.25 demonstrates the boundary layer thickness and displacement (Fn=0.6) at the section of the hull, where the capture area is positioned. Assuming the semi-elliptical shape for the capture area, the outline of the capture area is sketched as well. Since the boundary layer thickness is almost constant in transverse direction across the capture area, a single boundary layer profile can be used for obtaining the ingested momentum and energy flux. The boundary layer profile at the centreline of the capture area is the most reasonable boundary layer profile to select.

44
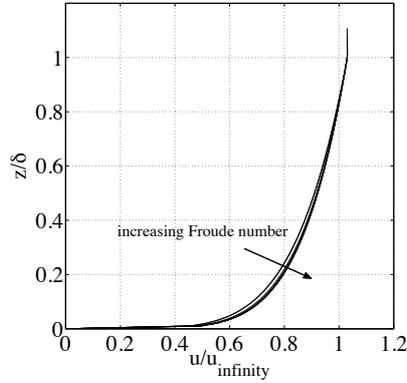
Figure 4.24 Boundary layer profile variation in different Froude numbers obtained at the centerline
of the capture area

According to Figure 4.25, at *Fn*=0.6, the height of the capture area is almost the same as the height of the boundary layer and the entire capture area may be assumed to be located inside the boundary layer. The height of the capture area decreases as the Froude number increases as seen in Figure 4.26.
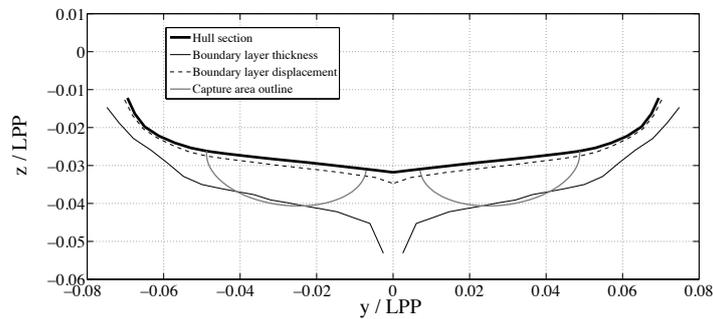
Figure 4.25 Illustration of the computed boundary layer thickness and displacement of a section
across the hull at the capture area at *Fn*=0.6

Since the capture area is mainly located inside the boundary layer, it is fair to assume that the velocity in this area is directed along the hull surface. By integrating the non-dimensional boundary layer velocity profile over the capture area and averaging it, the Intake Velocity Ratio (IVR), which may also be called wake fraction, is obtained. The variation of IVR versus the Froude number is plotted in Figure 4.27. Note the very large scatter in the experimental data.
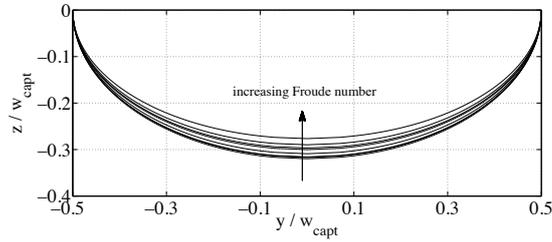
Figure 4.26 Semi-ellipsoid capture area geometry for different Froude numbers
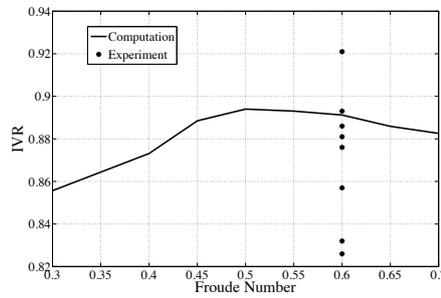
Figure 4.27 Non-dimensional mean velocity at the capture area (IVR)

The Nozzle Velocity Ratio (NVR) is provided in Figure 4.28. NVR shows the non-dimensional nozzle mean velocity. Due to the design of the nozzle discharge geometry for R/V ATHENA, the average pressure at the nozzle discharge is atmospheric and, therefore, there is no vena-contracta. In other words, NVR is equal to JVR (Jet Velocity Ratio). Although there is a hump in the NVR curve versus Froude number (Figure 4.28), the volume flow rate of the jet increases with Froude number (Figure 4.29). In both figures the predicted values fall within the bounds of the experimental scatter.
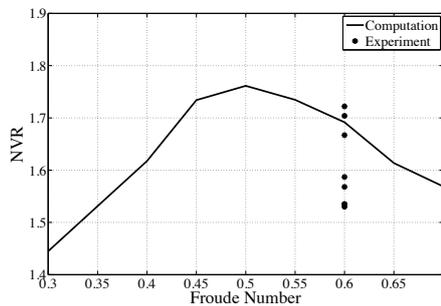
Figure 4.28 Non-dimensional nozzle mean velocity (NVR)

46
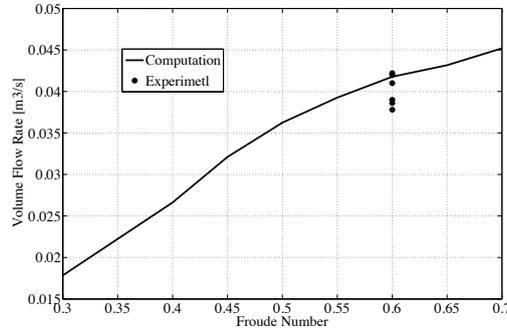
Figure 4.29 Volume flow rate through the ducting channel

The test results of the velocity profile in the nozzle discharge area show a considerable scatter, with the average bandwidth appearing to be 7%. It was reported that the longitudinal position of the measuring plane had a major effect on the velocity measured [28].

Obtaining the correct values for IVR and JVR is important for calculating the gross thrust. To check the importance of a correct JVR a sensitivity study may be made:

Considering a uniform distribution for the intake and jet velocity, it is possible to simplify Equation (3-5), for obtaining the gross thrust as follows:

$$T_g = \rho u_\infty^2 \cdot NVR \cdot A_8 (NVR - IVR)$$

(4-21)

According to Figure 4.27 and Figure 4.29, IVR and NVR at *Fn*=0.6 are:

$$IVR = 0.88, \quad JVR = 1.68$$

These IVR and NVR values will result in a certain gross thrust. If, for the same ship speed, IVR is assumed to be the same but NVR is reduced to 1.66 (about 1% less) the ratio of the gross thrust obtained from the new IVR and NVR and the old ones is as follows:

$$\frac{T_{g,2}}{T_{g,1}} = \frac{NVR_2 \cdot (NVR_2 - IVR_2)}{NVR_1 \cdot (NVR_1 - IVR_1)} = \frac{1.66(1.66 - 0.88)}{1.68(1.68 - 0.88)} \cong 0.96$$

(4-22)

This shows that a mere 1% under-prediction of the jet velocity results in 4% under-prediction of the gross thrust.

The computed bare hull resistance, net thrust and gross thrust (all corrected) are plotted in Figure 4.30 and compared with the measured gross thrust. Again, the computed gross thrust is within the experimental scatter. According to van Terwisga

47

[10], gross thrust and net thrust are very similar for most Froude numbers except for the hump region which is around Fn=0.6 for R/V ATHENA. However, this is not seen in the results of Figure 4.30. For Fn < 0.43 the gross thrust is smaller than the net thrust and for 0.43 < Fn it is vice versa. The maximum deviation is observed at Fn=0.6.
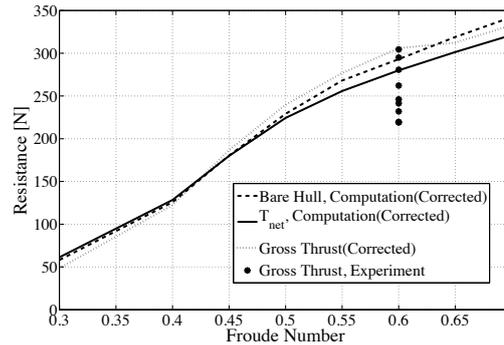
Figure 4.30 Bare hull resistance, net thrust and gross thrust variations

Figure 4.31 shows both total thrust deduction fraction t and resistance increment fraction, t_r (Equation (3-14)). Experimental data show the total thrust deduction fraction. Like in previous plots the corrected total thrust deduction fraction is within the experimental scatter. As mentioned earlier, corrected results show the curves obtained after applying the wave making resistance correction to the results of the potential flow solver. The measured thrust deduction fractions plotted in this figure is obtained from the measured model scale bare hull resistance and gross thrust. The corrected computed thrust deduction fraction shows a decent correspondence with the measured data.
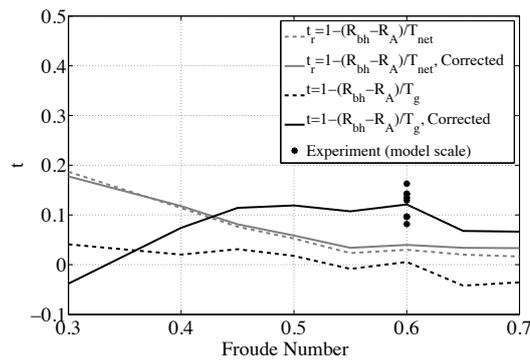
Figure 4.31 Thrust deduction fraction

48

5 Contribution of Different Parameters to Thrust Deduction

Conventionally, the total thrust deduction factor for a waterjet-propelled hull is defined as the ratio between the gross thrust of the waterjet system and the bare hull resistance. The gross thrust, in fact, is the horizontal component of the momentum flux change through the waterjet system. For a normal propeller, the thrust deduction factor is defined as the ratio between the net thrust and the bare hull resistance. The reason for introducing a different thrust deduction definition than that of conventional propellers is that there are some practical impediments in measuring the net thrust of a self-propelled hull, but it is much easier to measure the gross thrust of a waterjet unit. Measuring the force transmitted through the propeller shaft gives the net thrust of the propeller; but for the waterjet system, it is not only the impeller shaft, which transmits the thrust force to the hull; a proportion of the thrust is also transferred to the hull through the ducting channel. It is no easy task to measure this transmitted force. Instead, measuring the momentum flux change, which provides the gross thrust of the unit, seems more practical and achievable. In this chapter, based on the definitions of the net and gross thrust (Section 3.3), the possible parameters linking the bare hull resistance to the gross thrust of the self-propelled hull are identified. Then, the contribution of each of these parameters to the resistance of the hull is discussed. Knowing the magnitude of each single parameter separately helps to understand the physics behind the thrust deduction and may aid in the optimization of the hull/propulsor configuration. Also it may shed some light on the reason for the negative thrust deduction fractions sometimes found on waterjet driven hulls.

5.1 Flowchart Showing the Relation between Bare Hull Resistance and Gross Thrust

A summary of the items engaged in the thrust deduction analysis of a waterjet-propelled hull is presented in the flowchart given in Figure 5.1. It is the bare hull resistance and the gross thrust that finally needs to be compared. These two items appear on the top and bottom of the flowchart, respectively. All other items appearing in-between the bare hull resistance and the gross thrust are contributing to the total thrust deduction fraction.

The flowchart can be split into two major parts; the part connecting the bare hull resistance to the net thrust and the part relating the net thrust to the gross thrust. These parts define the thrust deduction fractions t_r and t_j (see Section 3.3), respectively.

Figure 5.1 Contribution of different parameters on thrust deduction of a waterjet propelled craft

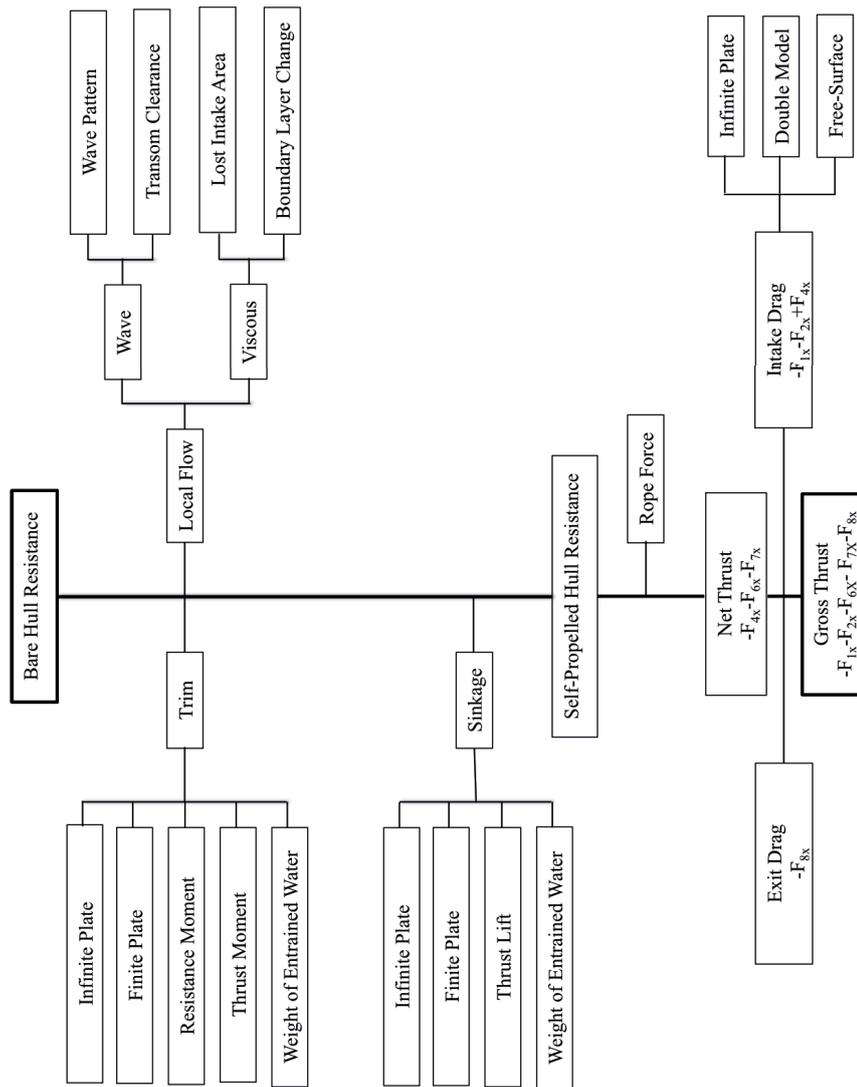As seen in Figure 5.1 the difference between the bare hull resistance and the self-propelled hull resistance is caused by three independent parameters, the changes of sinkage, trim and flow around the intake. The combined effect of sinkage and trim can be called global flow pattern change and the contribution of the flow change around the intake can be referred to as local flow change. Assuming that sinkage, trim and the local flow changes independently influence the resistance change, the resistance increment of the hull may be estimated from a linear expansion in a Taylor series and expressed as follows [10].

$$\Delta R(Q, d\sigma, d\tau) = \frac{\partial R}{\partial \sigma}(Q, 0, 0)d\sigma + \frac{\partial R}{\partial \tau}(Q, 0, 0)d\tau + \Delta R(Q, 0, 0) \qquad (\text{5-1})$$

The bare hull equilibrium position is the reference point, about which the Taylor expansion is made. Obtaining the partial derivatives of resistance with respect to sinkage, trim and flow rate individually, the contribution of each of them to the resistance increment may be estimated.

As mentioned in Chapter 4, at full scale the self-propelled hull resistance is equal to the net thrust, but at model scale a towing force, called rope force, is applied to the self-propelled hull to account for the too large frictional resistance. The net thrust is thus reduced by this force, as appears from Figure 5.1.

To further explore the influence of various parameters the sinkage, trim and local flow effects have been subdivided into different components in Figure 5.1. The occurrence and magnitude of these effects depends on the definition of the bare hull condition. *In this investigation the bare hull case is defined as a case where the propulsor has no influence on the sinkage, trim and local flow.* Thus the hull is pushed (or towed) horizontally at the height of the centre of effort of the resistance. In this way, the true effects of the propulsor on the resistance may be investigated. It should be stressed that this condition is somewhat theoretical, since neither propeller driven nor waterjet driven hulls normally satisfy these conditions. The effects of deviations from this ideal case in the bare hull testing will be discussed below.

Perhaps the most basic influence on the global effects, sinkage and trim, comes from the change in pressure distribution on the hull due to the waterjet intake, and the most fundamental case that can reveal such an influence is that of an infinitely large horizontal flat plate with an intake. The effect is denoted "Infinite Plate" in Figure 5.1, and the case is referred to as "free-stream condition" in the following. (In this condition there is also a duct attached to the intake ejecting the jet horizontally).

A more realistic case is obtained if only part of the infinite plate is considered. The part of the plate, with an area and beam similar to the hull in question, may be considered separately from the rest of the infinite plate, which thus represents the water surface. From the same solution as above the forces and moments on the "hull plate" can then be obtained. In the flowchart this case is referred to as "Finite Plate".

If the thrust is not horizontal, and applied at the same height as the resistance, a lift force and a trimming moment are created. The lift is denoted "Thrust Lift" in the flowchart. The moment is related to the centre of floatation and split into two components the "Resistance Moment" and the "Thrust moment", as will be further explained below.

The ducting system of the waterjet obviously contains water, not present in the bare hull case. This water will generate a vertical force and a moment on the hull thus altering the sinkage and trim. In the figure this effect is termed "Weight of Entrained Water".

It should be noted that if the bare hull is tested according to the ITTC recommendations, it is towed along the pump shaft axis, and the effect of the entrained water is taken into account by an additional weight at the stern of the hull. This is to approximately account for the inclined shaft and the entrained water already in the bare hull testing. Obviously the Thrust Lift, Thrust Moment and Resistance Moment for the self-propelled hull will then be much smaller, but they will not disappear entirely. Since the resistance of the self-propelled hull differs from that of the bare hull, there will be some contribution to all three. This contribution may be called a second order quantity and its magnitude is t_r times the first order quantity, i.e. it is one order of magnitude smaller than the first order quantity.

Due to the installation of the ducting channel, as well as the ingestion of the flow into the waterjet unit, some differences in the flow field in the aft part of the hull may occur in comparison to the flow field around the bare hull. This is called the "Local Flow" change and may have some impact on the increment of the resistance of the self-propelled hull. One may split the effect of the local flow change into the change taking place in wave making resistance and that taking place in viscous resistance.

The suction of the waterjet system results in a different wave pattern next to the aft part of the hull. The free surface is sucked down, and this may have different implications if the surface has a wave crest or a wave trough at this location. This effect is indicated as "Wave Pattern" in the flow chart.

As will be seen in Section 5.2 the suction of the water jet has several effects on the critical Froude number, where the transom clears the water. These effects may be quite important for the thrust deduction, particularly in the Froude number range where the transom is dry for the bare hull, but not for the self-propelled one. Effects of this kind are denoted "Transom Clearance" in the flow chart.

There are also some changes in the viscous flow around the hull. One may relate these viscous flow changes partly to the missing area of the bare hull surface, at the intake opening and partly to the boundary layer change in the vicinity of the intake due to the suction.

In the lower part of Figure 5.1 the effects relating net thrust and gross thrust are displayed. One component is the "Exit Drag" which occurs whenever the jet exit is submerged, or partly submerged, into the flow behind the transom. This situation occurs at low speeds, either when the water does not clear the transom or when the protruding part of the nozzle hits the (steep) stern wave.

Intake Drag is related to the forces on the protruding part of the control volume used in the momentum balance for obtaining gross thrust (See Figure 3.1). As will be seen below, this effect is zero under free-stream conditions, but not for a real case. The deviations from the free-stream conditions are denoted "Double Model" and "Free Surface", respectively.

5.2 Discussion of the Effects

In this section a more thorough discussion of the effects introduced in Section 5.1 will be presented. Wherever possible, formulas for estimating the effects will also be included. First the effects related to the global changes, sinkage and trim, will be discussed in Section 5.2.1. Thereafter effects of the local flow changes will be dealt with in 5.2.2 and finally the two effects responsible for the difference between net and gross thrust will be handled in 5.2.3.

5.2.1 Sinkage and Trim (Global Flow Effects)

Since similar effects influence sinkage and trim, they will be treated simultaneously in this section.

5.2.1.1 Infinite Plate

Referring to the control volume CV_1 in Figure 5.2, since the flow enters and leaves the control volume horizontally, there is no change in the vertical momentum flux inside CV_1. Hence, the sum of the vertical forces acting up on CV_1 is equal to zero.

53
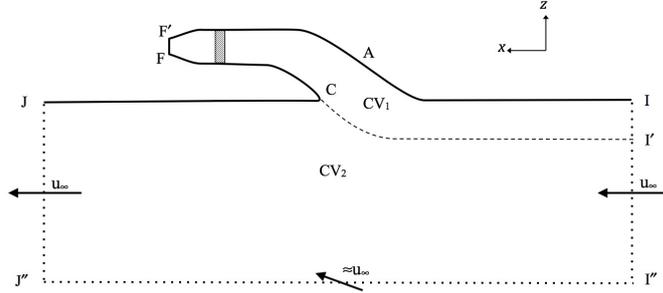
Figure 5.2 Control volumes used for derivation of intake induced lift

$$\sum_{CV_1} F_z = F_{z\,IAF'FC} + F_{z\,I'C} = 0 \qquad (\,5\text{-}2\,)$$

One can write the force balance for CV_2 as well; but since there is a normal flow through the lower part of the control volume CV_2, the sum of the forces in the vertical direction is not going to be zero. The mass flux, which enters CV_2 through surface I″J″, equals the discharged mass flux through surface FF′.

The momentum balance for CV_2 in the vertical direction is as follows:

$$\sum_{CV_2} F_z = F_{z\,CJ} + (-F_{z\,I'C}) = \phi_{mz\,I''J''} \qquad (\,5\text{-}3\,)$$

where $\phi_{mz\,I''J''}$ is the vertical momentum flux through surface I″J″.

Depending on the control volume, the sign of the force exerted on I′C, the common surface of CV_1 and CV_2, varies. The minus sign in front of $F_{z\,I'C}$ is applied to indicate that the sign of this force in CV_2 is different than the sign used in CV_1.

Summing Equation (5-2) and Equation (5-3) yields:

$$F_{z\,IAF'FC} + F_{z\,CJ} = \phi_{mz\,I''J''} \qquad (\,5\text{-}4\,)$$

The vertical momentum flux through the bottom surface may be expressed as:

$$\phi_{mz\,I''J''} = \int_{I''J''} \rho Q u_z dA \qquad (\,5\text{-}5\,)$$

At large distances from the intake the effect of flow in the intake may be approximated by a point sink, whose velocity disturbance decays quadratically with distance. Thus, for deep water, where the bottom surface may be considered infinitely far away, the velocity disturbance is zero. u_z is then identically zero over the whole integration range in Equation (5-5), which means that the vertical momentum flux $\phi_{mz\,I''J''}$ is zero. Equation (5-4) then shows that the sum of the forces on all material boundaries is zero. *There is no lift generated in free-stream conditions in infinitely deep water.* However, in shallow water, the vertical momentum flux $\phi_{mz\,I''J''}$ will not be zero, and subsequently there will be a lift force generated on the material surface.

The next step is an investigation of the infinitely large flat plate trim angle caused by the intake-induced pressure. The trim angle of a hull, τ, can be obtained from the following equation [43],

$$\tau = sin^{-1}\left(\frac{M_y}{\rho \nabla g \overline{GM_L}}\right) \times \frac{180}{\pi} \qquad (\,5\text{-}6\,)$$

where M_y is the trimming moment exerted on the hull; ρ is the water density and ∇ is the displacement volume if the hull. $\overline{GM_L}$ is the longitudinal metacentric height of the hull.

For a sufficiently long hull the longitudinal metacentric radius is so large compared to the distance between the centres of buoyancy and gravity that it may be considered equal to the longitudinal metacentric height, $\overline{GM_L} = \overline{BM_L}$. BM_L is obtained from,

$$BM_L = \frac{I_L}{\nabla} \qquad (\,5\text{-}7\,)$$

where I_L is the water plane area longitudinal moment of inertia.

Inserting Equation (5-7) into Equation (5-6) yields:

$$\tau = sin^{-1}\left(\frac{M_y}{\rho g I_L}\right) \times \frac{180}{\pi} \qquad (\,5\text{-}8\,)$$

Consider a flat plate of dimensions L x L (representing a hull) under which a constant positive pressure, $+p$, acts on one half (stern half) and a negative pressure, $-p$, on the other half (bow half). The moment, M_y, generated by the pressure around a line separating the two pressure distributions (around mid-ship) is:

$$M_y = 2 \times p \times \frac{1}{2} L^2 \times \frac{L}{4} = \frac{pL^3}{4}$$

(5-9)

The moment of inertia for the plate around the line in the middle (mid-ship) is:

$$I_L = L \times \frac{L^3}{12} = \frac{L^4}{12}$$

(5-10)

Using Equation (5-6) the trim angle of the plate hull will be:

$$\tau = sin^{-1}\left(\frac{12\,pL^3}{4\rho gL^4}\right) \times \frac{180}{\pi} = sin^{-1}\left(\frac{3\,p}{\rho gL}\right) \times \frac{180}{\pi}$$

(5-11)

In the limit of infinite L:

$$\lim_{L\to\infty} \tau = \lim_{L\to\infty} sin^{-1}\left(\frac{3\,p}{\rho gL}\right) \times \frac{180}{\pi} = 0$$

(5-12)

Since the trim angle for this generic case is zero for infinite L, this is certainly so for the more realistic pressure distribution, where the pressure is not constant, but decays with distance from mid-ship. Note that the limit is zero for any value of p, as long as it is finite.

5.2.1.2   Finite Plate

In this section, the lift force induced by the action of an intake positioned on a flat plate of a limited size is discussed. This case is thus closer to reality than the previous one. Figure 5.3 demonstrates the control volumes used for this analysis. The two control volumes introduced in this section differ from those used to study the infinitely large plate lift force. One of the control volumes, CV_3, includes the ducting channel and the other, CV_4, includes the rest of the flow. These control volumes share a common surface, which is the imaginary surface covering the intake opening. Accordingly, when writing the force balance for each of the control volumes, it should be kept in mind to set different directions for the force on this surface. Note that CV_4 extends to infinity in all directions except upwards.
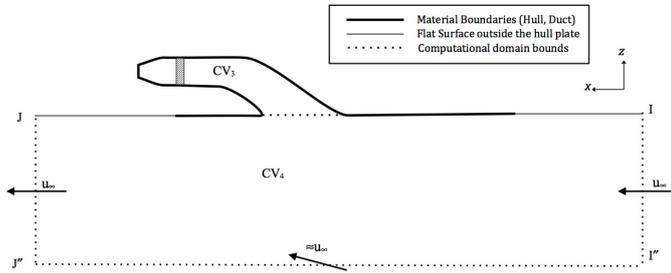
Figure 5.3 Control volumes used for derivation of intake induced lift on a finite flat plate. The solid line shows the flat plate and the dashed line demonstrates the employed control volume.

The control volumes, CV_3 and CV_4 are separately demonstrated in Figure 5.4 and Figure 5.5. Moreover, the forces exerted on each of these control volumes are indicated. The positioning of the forces in these figures is merely for demonstration and does not imply the location where the forces are exerted in reality. These forces are defined as follows:

F_D : vertical force exerted by the ducting channel.

F_I : vertical force exerted on the imaginary surface covering the intake opening.

F_H : vertical force exerted on the flat plate representing the hull bottom.

F_O : vertical force exerted on the flat surface outside of the hull bottom.

$F_S : F_S = F_H + F_O$.
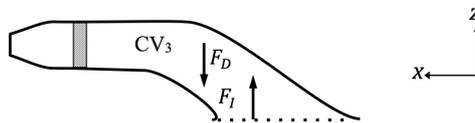
Figure 5.4 Control volumes, CV_3, and the vertical forces exerted thereon.
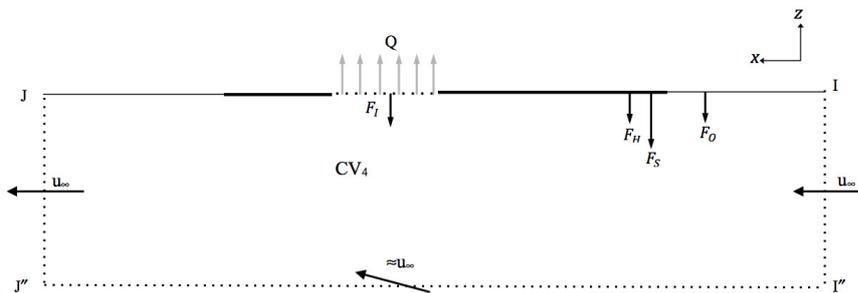
Figure 5.5 Control volumes, CV_4, and the vertical forces exerted thereon.

Writing the momentum flux balance for the control volume CV_4 in the vertical direction results in:

$$\phi_{Iz} - \phi_{I''J''z} = -F_I - F_S \qquad (5\text{-}13)$$

where ϕ_{Iz} and, $\phi_{I''J''z}$ are the momentum fluxes in the z-direction through the intake and bottom surface of CV_4. Since the bounds of the control volume are stretched into infinity, there is no normal velocity through the bottom surface of CV_4. As seen in the previous section, the vertical momentum through the bottom surface is zero in deep water

$$\phi_{I''J''z} = 0$$

Therefore, Equation (5-13) simplifies to the following equation.

$$\phi_{Iz} = -F_I - F_S \qquad (5\text{-}14)$$

This equation implies that the momentum flux through the intake is equal to the sum of all forces exerted on the entire horizontal plane, including the imaginary surface covering the intake opening.

Writing the same momentum balance for CV_3 gives the following equation:

$$\phi_{FF'z} - \phi_{Iz} = -F_D + F_I \qquad (5\text{-}15)$$

Since it is assumed that the jet is discharged horizontally, there is no component of the jet momentum flux in the vertical direction;

$$\phi_{FF'z} = 0$$

thus, Equation (5-15) may be simplified into the following equation:

$$-\phi_{Iz} = -F_D + F_I \qquad (5\text{-}16)$$

Adding Equations (5-14) and (5-15), the combined result is:

$$F_D = -F_S. \qquad (5\text{-}17)$$

Subsequently, replacing the duct geometry with the resultant force exerted on it one may express the duct/flat plate hull system as in the free body diagram shown in Figure 5.6.

Figure 5.6 Duct/flat plate hull free body diagram.
(Forces act on the solid surfaces, not the flow)

The duct force, F_D, should be applied to the centre of the duct force. Taking a look at Figure 4.17 and Figure 4.18, which show the pressure distribution inside the ducting channel, applying this force at the same position as the trailing edge of the intake opening would be a decent assumption.

The intake-induced sinkage, σ_0, due to the forces exerted on the duct/hull system may now be obtained as:

$$\sigma_0 = \frac{F_D + F_H}{\rho g A_H}$$

(5-18)

where A_H is the water plane area of the hull.

Moreover, one can estimate the trim angle of the hull due to intake induced pressure and the duct force [43]:

$$\tau_0 = sin^{-1}\left(\frac{M_{D\,y} + M_{H\,y}}{mg\overline{GM}_L}\right) \times \frac{180}{\pi}$$

(5-19)

where $M_{D\,y}$ and $M_{H\,y}$ are the moments created by the ducting channel and hull, respectively, about the y-axis. m is the hull mass and $\overline{GM}_L$ is the longitudinal metacentric height of the hull.

Since the flat plate representing the hull is rectangular, the natural pivot point would be in the middle of the plate, not the location of the pivot point in reality. In order to correct this problem, the pivot point is moved to the real pivot point position on the real hull, which is the centre of floatation of the hull.

5.2.1.3   Thrust and Resistance Effects on Sinkage and Trim

Figure 5.7 shows a waterjet propulsion system with an inclined nozzle. The angle of nozzle inclination, θ_n, shows the inclination of the shaft line from the horizontal plane. This angle can be attributed to the design of the ducting channel and/or trim angle of the hull. The total inclination of the nozzle is obtained by adding the hull trim angle, τ, to the nozzle design inclination angle as shown in Figure 5.7. The

entire thrust of the waterjet unit is supposedly transmitted through the shaft. In case of thrust force inclination, a component of the force would be in the vertical direction, which causes the hull to rise. The change in the sinkage of the hull due to the inclination of the nozzle can be obtained as follows:

$$\sigma_T = \frac{T_Z}{\rho g A_H} \tag{5-20}$$

where T_Z is the vertical component of the total thrust force and A_H is the water plane area of the hull.
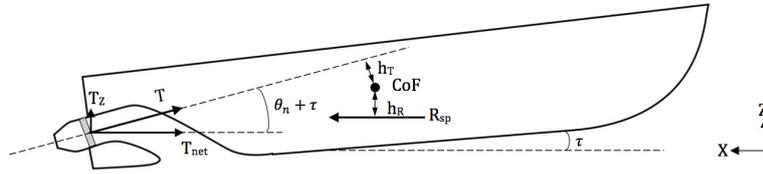
Figure 5.7 Illustration of Waterjet propelled hull with an inclined nozzle

Moreover, there will be two trimming moments about the centre of floatation due to the resistance and thrust forces. These moments can be calculated from the following equations:

$$M_{Ty} = T \times h_T \tag{5-21}$$

and,

$$M_{Ry} = R_{sp} \times h_R \tag{5-22}$$

where M_{Ty} and M_{Ry} are thrust, T, and resistance, R$_{sp}$, trimming moments, respectively. h$_T$ and h$_R$ are the lever arms, which are depicted in Figure 5.7.

Trim angle of the self-propelled hull due to latter trimming moments can be calculated as follows:

$$\tau_T = sin^{-1}\left(\frac{M_{Ty}}{mg\overline{GM}_L}\right) \times \frac{180}{\pi} \tag{5-23}$$

and,

$$\tau_R = sin^{-1}\left(\frac{M_{Ry}}{mg\overline{GM}_L}\right) \times \frac{180}{\pi} \tag{5-24}$$

where τ_T and τ_R are trim angles due to thrust and resistance forces, respectively. m is the hull mass, g is the gravitational acceleration and $\overline{GM}_L$ is the longitudinal metacentric height of the hull.

According to these definitions, larger nozzle inclination causes the hull to rise and trim less (more bow-down). Thus, the effect of nozzle inclination on sinkage and trim of small boats which may achieve large trim angles will be more pronounced compared to large hulls with smaller trim angles and more often no nozzle inclination in the original design of the waterjet unit.

5.2.1.4   Weight of the Entrained Water

According to the model test procedure proposed by the 24th ITTC Waterjet Specialist Committee [44], during the resistance test, the entrained water is represented by a load to create a better correlation between the bare hull and self-propelled hull initial sinkage and trim. The load, which is used to compensate the weight of the entrained water in a static equilibrium condition, is equal to the weight of the water inside the ducting channel. It is not clear whether the water weight is to be computed for the total duct volume or only up to the water level in zero speed. The latter volume is shown in grey in Figure 5.8
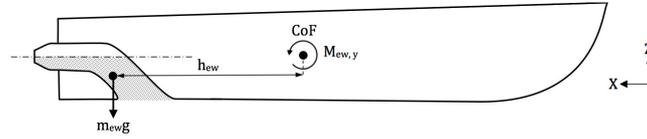
Figure 5.8 Illustration of the entrained water and its moment applied to the hull

The effect of the total amount of entrained water on the hull sinkage can be obtained through the following equation in which the subscript EW stands for entrained water:

$$\sigma_{EW} = \frac{m_{EW}g}{\rho g A_H} \qquad (5\text{-}25)$$

where m_{EW} is the weight of the total entrained water.

Moreover, the trim angle can be calculated as:

$$\tau_{EW} = sin^{-1}\left(\frac{M_{EW\,y}}{mg\overline{GM}_L}\right) \times \frac{180}{\pi} \qquad (5\text{-}26)$$

where $M_{EW\,y}$ is the moment created by the weight of the water inside the ducting channel.

$$M_{EW\,y} = m_{EW}g h_{EW}$$

(5-27)

h_{EW} is the horizontal distance between the centre of gravity of the total entrained water and the centre of floatation of the hull depicted in Figure 5.8.

5.2.2   Local Flow

In this section the intake induced effects on the local flow will be discussed.

5.2.2.1   Waves

Depending on whether a wave crest or a wave trough occurs next to the intake, the wave making resistance may decrease or increase, because the waterjet unit sucks down the nearby flow. If a wave crest occurs in the vicinity of the intake, it becomes flatter and, therefore, wave making resistance decreases. In contrast, if a wave trough occurs in this region, the intake sucks it down and the wave becomes steeper, which naturally increases the wave making resistance of the hull. For high-speed craft, it is more probable to have the wave trough than wave crest in the aft part, which leads to the conclusion that the waterjet system normally increases the wave making resistance of the hull. An example is presented in Figure 5.9 showing a wave cut just beside the hull for the Athena hull at a Froude number of 0.6, bare-hull and self-propelled. The hull is located between 0 and 1 in the plot, and it is clearly seen that the wave trough is sucked down by the waterjet, which increases resistance.
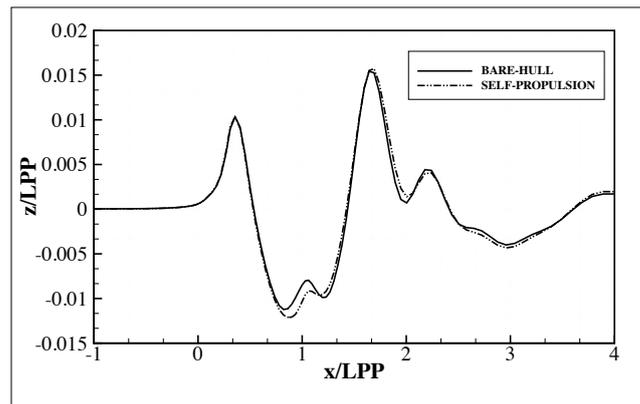
Figure 5.9 Wave cut profile comparison at $\frac{y}{LPP} = 0.085$ for R/V ATHENA at Fn=0.6. The hull is located in $0 \leq \frac{x}{L} \leq 1$.

The other waterjet influence on the waves, as seen in Figure 5.10, is the effect on the transom clearance. In fact, there are several reasons for this influence. Figure 5.10 shows a very simplified 2-D transom geometry, without a water jet, with an intake, and with an intake and a jet. The flow solution was obtained using a viscous flow solver (FLUENT) and shows the basic effects. First it is seen that the intake generates an up-flow near the transom edge, which causes the initially horizontal free surface, located at the bottom of the hull, to raise behind the hull. Second, when the jet is introduced the transom becomes wetted. For a real 3-D case this indicates that the wave behind the hull becomes steeper due to the suction, which makes it more unstable. The larger steepness is clearly seen in the potential flow solution for the ATHENA hull in Figure 5.9. A higher Froude number might then be expected for the transom to clear the water, i.e. to get a small enough wave slope to avoid breaking and the subsequent filling of the zone behind the hull with dead water. This effect may be enhanced by the (related) fact that the flow under the hull, behind the intake, is slowed down relative to the bare hull case. A water jet driven hull is thus likely to clear the transom at a higher Froude number than the bare hull. This may have a significant effect on the thrust deduction in a Froude number range where the transom is cleared for the bare hull, but not for the self-propelled one.

a. blocked intake / blocked jet   b. active intake / blocked jet

c. active intake / active jet
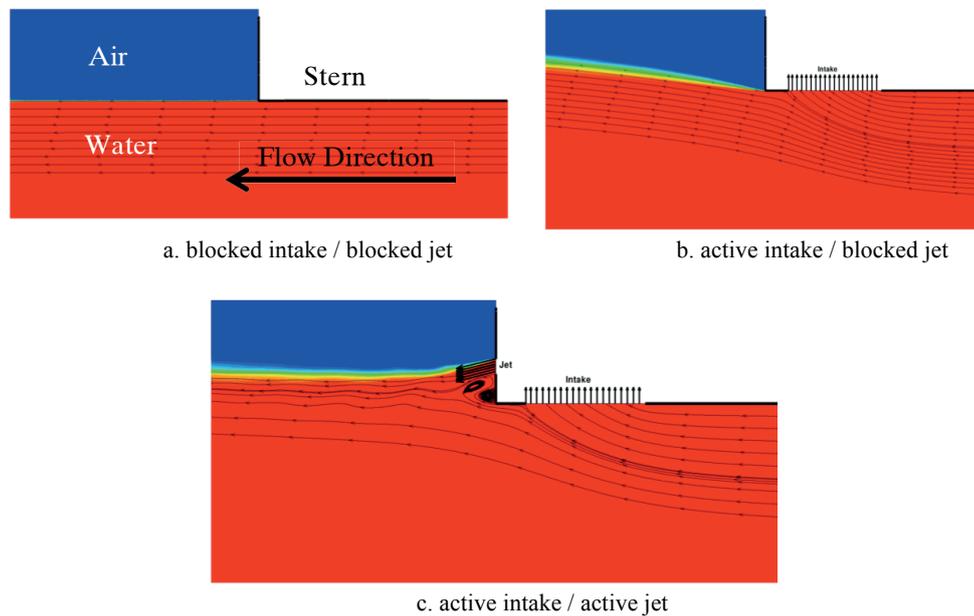
Figure 5.10 A simplified two-dimensional CFD simulation of transom flow

5.2.2.2   Viscous Resistance

Removing the intake-covering surface on the self-propelled hull obviously decreases the frictional resistance, but it should be kept in mind that a new boundary layer starts to grow after the trailing edge of the intake, which may increase the frictional resistance. Moreover, the negative pressure gradient and increased velocity change the boundary layer development and increase the frictional resistance of the hull in front of the intake. The net effect of the boundary layer change is thus likely to be an increase resistance.

5.2.3   Relationship between Net Thrust and Gross Thrust

In previous sections, the relationship between the bare hull resistance and the net thrust has been discussed. But in practice, it is the relationship between the bare hull resistance and the gross thrust that is being employed to design a waterjet unit of a specific hull. Thus, the relationship between the net thrust and the gross thrust is also required to link the bare hull resistance to the gross thrust. According to Equation (3-7) the relation between gross and net thrust may be written:

$$-\text{T}_g = -\text{T}_{net} + \iint\limits_{A_1+A_2+A_8} \sigma_x dA - \iint\limits_{A_4} \sigma_x dA \qquad\qquad (\,3\text{-}7\,)$$

The integrals over the surfaces A_1, A_2 and A_4 together define the intake drag, Di

$$\text{D}_i = -\iint\limits_{A_1+A_2} \sigma_x dA + \iint\limits_{A_4} \sigma_x dA \qquad\qquad (\,5\text{-}28\,)$$

while the integral over the surface A_8 defines the exit drag, D_e:

$$\text{D}_e = -\iint\limits_{A_8} \sigma_x dA \qquad\qquad (\,5\text{-}29\,)$$

Thus

$$\text{T}_g = \text{T}_{net} + D_i + D_e \qquad\qquad (\,5\text{-}30\,)$$

van Terwisga [10] shows that the intake drag is zero for free-stream conditions However, for operational conditions it will not be zero for several reasons:

64

- The intake velocity is not undisturbed.
- There is a pressure gradient along the surface A_2 caused by the finite dimensions of the hull.
- There is a pressure gradient along the surface A_2 caused by the free surface waves.

The first effect was quantified by van Terwisga in potential flow, but his relation cannot be applied in viscous operational conditions. A more thorough investigation of the three effects under operational conditions should be most valuable.

The exit drag is zero if the pressure at the jet exit is atmospheric. This is the case for normal water jets, where the centre of the jet is at the water plane, provided the speed is high enough. At very low speed the water does not clear the transom and the nozzle exit is partly below the surface in the dead-water zone. There is thus a hydrostatic pressure over part of the exit. When the speed increases, the water will clear the transom, but if the speed is not high enough the stern wave may be so steep that the nozzle protrudes the wave, resulting in a disturbed exit pressure. For a sufficiently high speed the wave slope becomes large enough for the exit to be entirely in the air, and the exit drag is zero.

5.3   Examples

In this section the various contributions to the sinkage and trim changes due to the waterjet action are estimated and compared to those obtained from numerical simulations or experiments. Thereafter, the resistance increment (Equation (5-1)) of the hull is obtained. It should be stressed that these computations are not intended to be quantitatively accurate; they are made to investigate the relative importance of the various factors in a qualitative way.

5.3.1   Free-Stream Sinkage and Trim Estimation

5.3.1.1   The Finite Plates

In order to estimate the free-stream sinkage and trim, the induced lift force and moment due to the waterjet suction are obtained in a potential flow for a very large flat plate (approximating an infinitely large plate). A constant distribution of normal velocity on the simplified rectangular shape of the intake area is assumed. Two different flat plate hulls with different intake sizes are created as parts of the very large plate. The size of the flat plate hulls should approximate the size of R/V ATHENA and HAMILTON jet boat bottom surfaces. The characteristic data of R/V ATHENA and HAMILTON jet boat geometries are provided in Section 4.3.1 and Appendix C, respectively. These hulls are of different types with very different characteristics. A sketch of the flat plates and the intakes are provided in Figure 5.11 and Figure 5.12 and the related dimensions are specified in Table 5.1. The width of the plate is equal to the max beam of the waterline of the hull and the length is computed to give approximately the same water-plane area as the hull. This should give reasonable estimates of the sinkage, while the trim will be somewhat over-predicted due to the too small moment of inertia of the plate. Note that the Athena hull is at model scale, while the Hamilton case is at full scale.
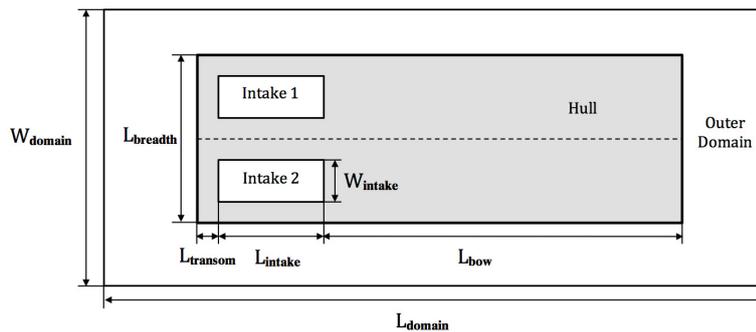

Figure 5.11 General sketch of the computational domain for the flat plate representing R/V ATHENA
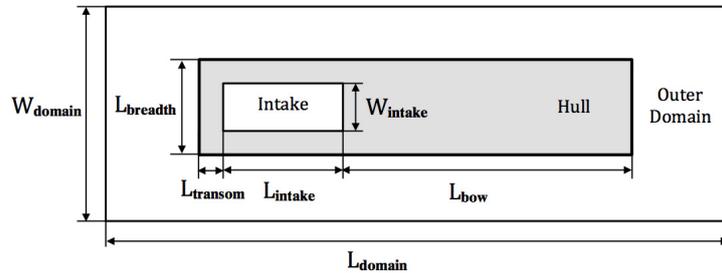
Figure 5.12 General sketch of the computational domain for the flat plate representing HAMILTON jet boat

Table 5.1 Characteristic dimensions of the flat domain employed to simplify the actual hull geometries

	L_{intake}	W_{intake}	L_{bow}	$L_{transom}$	$L_{breadth}$	L_{domain}	W_{domain}
R/V ATHENA	0.31	0.17	4.69	0.23	0.70	60	40
HAMILTON jet boat	0.70	0.35	4.80	0.19	2.20	60	40

* All lengths are in meters.

As a first step, the error of the numerical simulation due to non-infinite domain size should be investigated. According to the momentum balance over CV_4 shown in Figure 5.3, for an infinitely large domain, the momentum flux through the intake is equal to the force exerted on the flat plate including the intake area (Equation (5-14). But since there is no possibility to simulate an infinitely large domain in the numerical calculation, the size of the flat plate must be limited. Different sizes of outer domain were tested to investigate the effect of domain size on the satisfaction of Equation (5-14). Eventually, the computational domain length, L_{domain}, and width, W_{domain}, indicated in Table 5.1, were selected. The percentage of the lift force to momentum flux ratio in percent for each of the hulls is provided in Table 5.2. The deviation from 100% is due to the limited size of the domain and the numerical discretization. Since the deviation is very small the errors can be assumed negligible. It should be noted that the density of the panels close to the intake edges is very important for the calculated lift force, the reason being the large pressure gradients occurring close to the intake.

Table 5.2 The induced lift force ratio to the momentum flux through intake

	$(F_I + F_H + F_O)/\phi_I$ %
R/V ATHENA	98.57
HAMILTON jet boat	98.14

67

The panelization for the flat plate domains, including the intake, hull and outer domain as well as the obtained pressure distribution due to the suction, is presented in Figure 5.13 to Figure 5.18 for both cases. The total number of panels on the large flat surface are almost 18000 and 13000 and the intake velocity ratio, IVR $_I$, is set to be 0.23 and 0.21 for the R/V ATHENA and HAMILTON jet boat, respectively. These IVR $_I$ ratios are appropriate for the self-propulsion point at $Fn \cong 0.6$ for both hulls.

Figure 5.13 Panelization of the planar computational domain for R/V ATHENA

Figure 5.14 Closer look at the panelization of the flat hull of R/V ATHENA

Figure 5.15 Pressure distribution on the flat plate representing R/V ATHENA
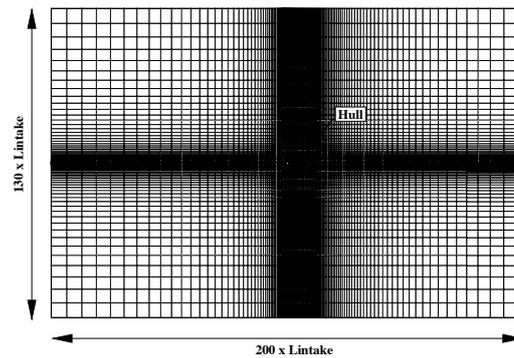
68

Figure 5.16 Panelization of the planar computational domain for the HAMILTON jet boat
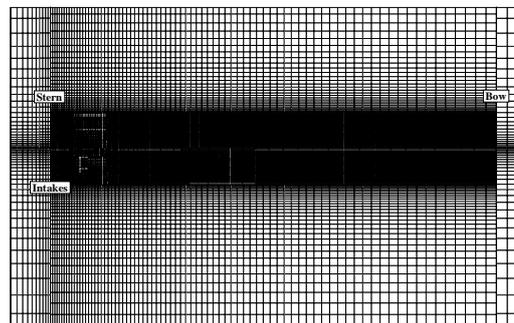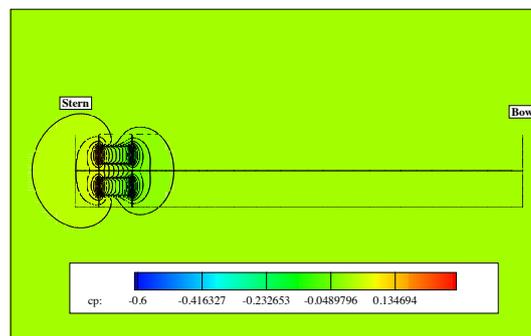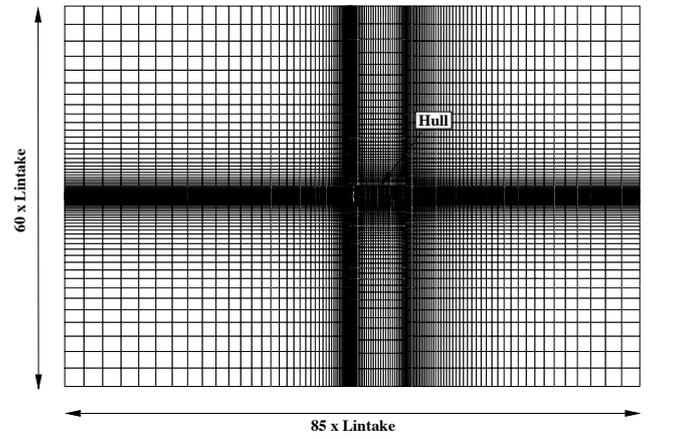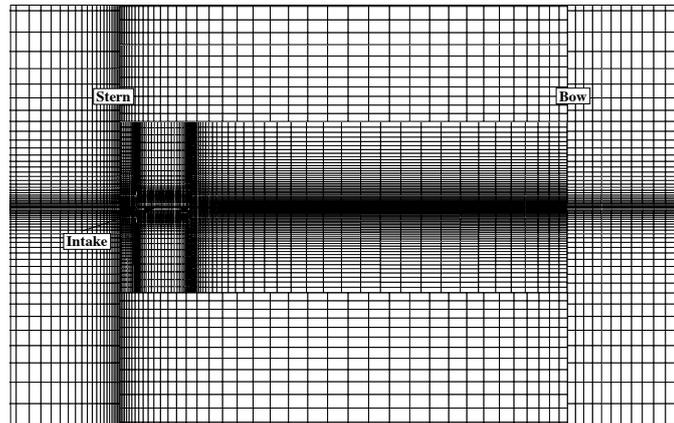

Figure 5.17 Closer look at the panelization of the flat hull of the HAMILTON jet boat
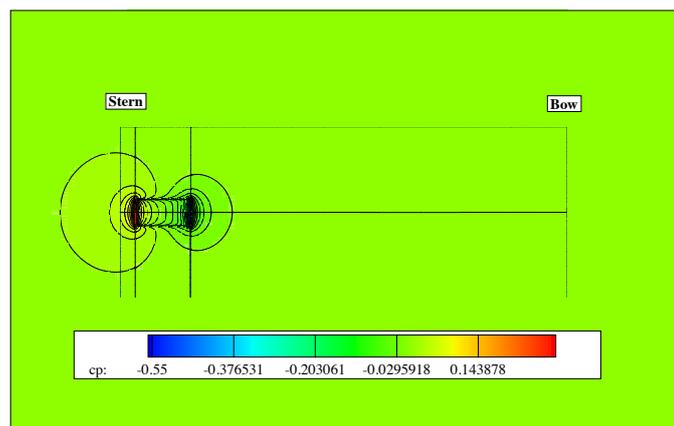
Figure 5.18 Pressure distribution on the flat plate representing the HAMILTON jet boat

According to Figure 5.15 and Figure 5.18, the pressure in front of the intakes is lower than the undisturbed pressure while it is higher behind the intake. Depending on the size of the hull, some proportion of these low-pressure or high-pressure zones may lie outside the hull which has an effect on the lift force and moment on the hull. In the following section, the effect of different hull sizes on the lift force and moment exerted on the hull will be discussed.

5.3.1.2   Sinkage and Trim Estimation

In order to obtain the lift, moment and their resultant sinkage and trim angle, the procedure suggested in section 5.2.1.2 is employed. Basically, a single force representing the duct force is added to the force from the pressure distribution obtained from the flat plate simulation; the resultant force and moment is then calculated for varying hull sizes. The forepart, aft part and width of the hull are extended separately. For instance, if the aft part of the hull is extended, both the size of the forepart and width of the hull are kept the same as the standard hull size.
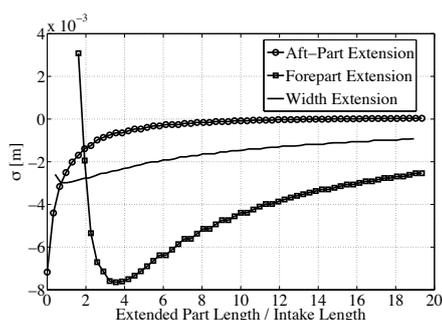
Figure 5.19 Sinkage variations by extending the flat plate in different directions (R/V ATHENA)
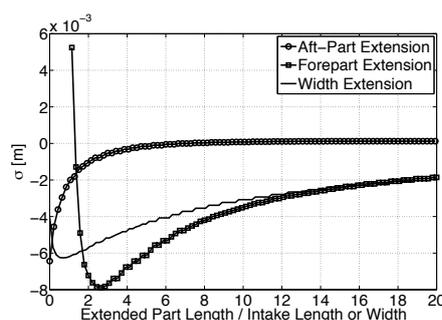
Figure 5.20 Sinkage variations by extending the flat plate in different directions (HAMILTON jet boat)

Figure 5.19 and Figure 5.20 demonstrate the sinkage variation of the hull in the free-stream condition by extending the flat plate in different directions for cases representing both the R/V ATHENA and the HAMILTON jet boat. Extending all directions causes the sinkage to converge to a certain value. The interesting point is that this certain value is almost zero for the extension of the aft part of the hull but not in the case of extending the other part of the hull. The reason is that almost all the waterjet intake induced pressure is located on the hull for the standard hull sizes except for some zones of high pressure located in the aft part of the hull (see Figure 5.15 and Figure 5.18). Extending the hull plate in any direction other than the aft part will not induce much upward lift while the low-pressure region ahead of the intake generates a lift force (pointing downwards), causing the hull to sink.

70

Recovering the high pressure in the aft part of the hull by extending it may control the sinkage of the hull and may be taken into account in designing the vessel.

According to section 5.2.1.1, there is no lift force for infinitely large flat plates in the free-stream condition, but the results obtained in Figure 5.19 and Figure 5.20, the conclusion for a flat plate of limited size may differ depending on the extent to which the hull covers the regions with distorted pressure due to the intake suction. For a flat plate of the size of a normal hull and standard intake positioning, the lift force (pointing downwards) causes the hull to sink. The resultant sinkage is caused by the pressure distribution on the hull, in addition to the ducting channel force. Furthermore, there is one additional factor to be taken into account to estimate the absolute sinkage of the hull, the inclination of the nozzle that may result in an additional lift force, an effect that was introduced in session 5.2.1.3.
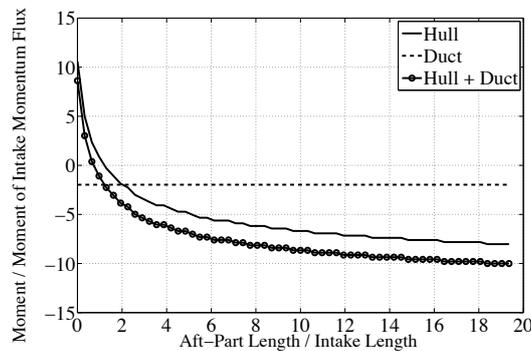
Figure 5.21 Contribution of different forces on the momentum exerted on the flat plate representing R/V ATHENA

Figure 5.21 shows the moment exerted on the hull by extending the aft part of the flat plate representing R/V ATHENA. An aft part length equalling zero means that there is no surface belonging to the hull after the intake trailing edge. Since the duct force for a certain intake velocity ratio (Equation (5-17)) is constant, the moment created by the duct force does not vary. The only varying moment is that created by the pressure distribution on the flat plate. Increasing the length of the aft part of the hull, a larger region with high pressure is located on the hull. This increases the bow down moment rapidly but after extending the hull for a certain length, the bow down moment does no longer increase and converges to a certain value caused by the fact that no distortion on the flat plate pressure can be detected far downstream of the intake.

Figure 5.22 and Figure 5.23 depict the trim angle variation of the flat plates representing R/V ATHENA and HAMILTON jet boat, respectively. Similar to sinkage plots, the horizontal axis shows the extension of the flat plate in a certain

71

direction. Equation (5-19), in combination with computed moments exerted on the flat plate, is used to obtain these figures. For both plates, the extension of the hull in any of three directions results in a zero trim angle. This is in agreement with the proof in Section 5.2.1.1 that the trim is zero for free-stream conditions in deep water. The reason is that the extension of the hull beyond a certain region, where no noticeable distorted pressure exists, does not change the exerted moment on the hull (see Figure 5.21) but rather increases the metacentric height, which appears in the denominator of Equation (5-19) and causes the trim angle to converge to zero.
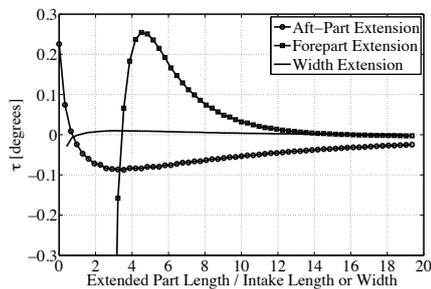
Figure 5.22 Trim angle variations by extending the flat plate in different directions (R/V ATHENA)
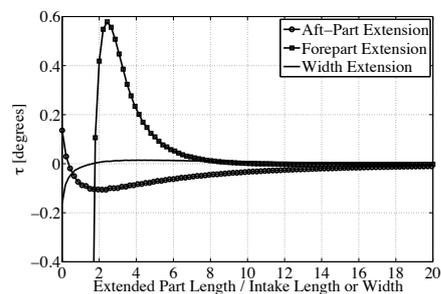
Figure 5.23 Trim angle variations by extending the flat plate in different directions (HAMILTON jet boat)

Comparing the curves demonstrating the extension of the forepart or aft-part of the flat plate, the trim angle does not seem to be sensitive to the extension of the flat plate width. The reason is that the pattern of the pressure distribution on the plate is almost symmetric to the symmetry axes of the intake (see Figure 5.15 and Figure 5.18). Increasing the plate width practically covers the same low-pressure as high-pressure regions, which balance each other so that no moment is exerted on the hull.

The extension of the forepart seems to greatly affect the hull trim angle in the beginning but rapidly dampens out. For the R/V ATHENA and HAMILTON jet boat, the standard ratio of the forepart length to the intake length is around 15 and 9, respectively. This means that a flat plate of standard size for a normal hull will not experience the extreme changes in the trim angle as shown in forepart extension curves in Figure 5.22 and Figure 5.23

After studying the effect of the hull size in free-stream condition on the sinkage and trim of the hull, the sinkage and trim for the flat plate in free-stream condition of the size closest to the R/V ATHENA and HAMILTON jet boat test cases have been obtained. Thereafter the other effects discussed in sections 5.2.1.2 to 5.2.1.4 have been computed, i.e. the effects of the thrust lift and moment, resistance moment and entrained water weight. Table 5.3 and Table 5.4 show the contribution of each of these parameters on the sinkage and trim change. Also, after the various

contributions the total value from the computational simulation for R/V ATHENA and experimental data available for the HAMILTON jet boat are presented. These computed/measured values are indicated by "'actual' in the tables. The reason for not showing both computed and experimental total values for both hulls is that the measured data for Athena (from the ITTC measurements) are so scattered that it is even difficult to determine the sign of the effects, while the Hamilton case could not be computed due to lack of some important data for the case.

Table 5.3 Contribution of different effects on sinkage change
(First order quantities shown).

$$\Delta\sigma \left(\sigma_{sp} - \sigma_{bh}\right) [mm]$$

	R/V ATHENA	HAMILTON JET BOAT	
Fn	0.60	0.62	0.98
Finite plate	-3.0	-4.3	-9.2
Thrust lift	+0.15	+6.6	+8.8
Entrained Water	-3.3	-4.7	-4.7
Actual	-2.9	-2.1	22.8

Table 5.4 Contribution of different effects on trim angle change.
(First order quantities shown).

$$\Delta\tau \left(\tau_{sp} - \tau_{bh}\right) [°]$$

	R/V ATHENA	HAMILTON JET BOAT	
Fn	0.60	0.62	0.98
Finite Plate	0.00	+0.01	+0.03
Thrust Moment	-0.01	-0.51	-0.67
Resistance Moment	-0.03	-0.21	-0.24
Entrained Water	-0.23	+0.33	+0.33
Actual	-0.02	-0.05	-0.47

Since the tests were carried out according to the ITTC procedure for both hulls, only the second order values of the Thrust Lift and Moment, Resistance Moment and Entrained water will influence the total value, i.e. only the changes in these parameters between the bare hull and self-propulsion will be of importance. As explained above, the first three are obtained by multiplying the first order values in the table by t_r. The magnitude of the fourth is not known due to lack of information on the computation of the entrained water effect in the measurements. If the volume above the still waterline at zero speed was included when computing the entrained water weight, there would be no change at self-propulsion and the effect would be zero in the table, but if this volume was not included there will be some effect.

As seen in Figure 5.19 the flat plate sinkage for ATHENA corresponds very well with the computed total sinkage change. There is no contribution from the second

order Thrust Lift, since the only inclination of the shaft is due to the small trim angle. Assuming that the total entrained water had been considered in the bare hull tests (so that the contribution in the table would be zero) it can be concluded that the sinkage is almost entirely due to the change in pressure distribution around the intake. With the same assumption for the Entrained Water all second order quantities are virtually zero. The Finite Plate indicates no trim change, and the actually computed value for the hull is also practically zero, - 0.02 degrees. So, the hull does not trim since the change in the pressure distribution around the intake generates zero moment, as seen in the flat plate results.

For the Hamilton hull there are two Froude numbers. In both cases there will be some effect of the second order quantities. The thrust deduction fraction t_r is not known at these Froude numbers, but the total thrust deduction t is around - 0.05. Assuming that the influence of t_j is very small (as conjectured by van Terwisga [10]), the real effects of the Thrust lift and Moment and the Resistance Moment are - 5% of the first order values in the tables. Assuming again that the total volume of entrained water has been considered in the bare hull tests the sum of the effects for the sinkage at the low Froude number would be - 4.0 mm, while the measured on is - 2.1 mm. The trim change would be very small, about – 0.01 degrees, as compared with small the measured value – 0.05 degrees. A similar conclusion for this case as for the ATHENA may be drawn for the trim: the pressure changes around the intake generate practically no trim at this Froude number. The over-prediction of the sinkage change by the flat plate may be due to the flat plate approximation. One must not overstress the results of this simple approach.

For a given IVR, the flat plate results should be proportional to the Froude number squared. Now, for HAMILTON, the IVR is slightly smaller for the higher Froude number, so the increase in sinkage between the Froude numbers is slightly smaller than quadratic: it increases from -4.3 mm to -9.2 mm. Adding the second order thrust lift, a sinkage change of – 9.6 mm is obtained. This should be compared with a measured value of – 22.8 mm. Like for ATHENA there is thus a factor 2 between the estimated and actual values, but here the estimated value is the smallest. The HAMILTON results are more cumbersome, since the sinkage increases 10 times between the Froude Numbers in the measurements, which indicates that the waterjet induced pressure is not the cause of the change. This requires further investigation. There is also a question mark for the trim. While the estimated value considering the second order effects is practically zero, -0.01, the actual value is quite large, -0.47.

The sinkage and trim changes appear to be mainly due to the changes in pressure distribution around the intake, as approximated by the flat plate computations, for the ATHENA hull and the HAMILTON jet boat at the low Froude number.

However, at the higher Froude number the measured changes cannot be explained in this way. Further investigations of this problem are needed.

5.3.2 Resistance Increment Estimation

As introduced in Section 5.1, the resistance increment of the hull is a function of three independent variables: the hull sinkage, trim and the flow rate through the waterjet system. Derivatives of the hull resistance with respect to each of these variables are given on the right hand side of Equation (5-1). In the following, the magnitude of the sinkage, trim and local flow change effect on the hull resistance increment will be estimated for R/V ATHENA.

To get started with this investigation, the self-propelled hull equilibrium position was set to the reference sinkage and trim obtained from the bare hull simulation. Thereafter, one of the parameters sinkage, trim or flow rate was varied while the other two were kept fixed as reference points. This procedure was accomplished for all three parameters. In order to make the sinkage and trim variations totally independent, the sinkage needs to be measured at the centre of floatation (CoF), where the hull does not change its displacement due to trimming. Going through this procedure provides three curves for resistance variations depending on variations of the sinkage, trim and flow rate. The curves obtained for R/V ATHENA are shown in Figure 5.24, Figure 5.26 and Figure 5.29, respectively. The effect of the flow rate variation on the resistance change is studied by NVR variations. Since the variation of the parameters are accomplished for some discrete points, to obtain a smooth curve for the derivatives, one needs to obtain the curve which fits the discrete points and then obtain the derivative of the smooth curve. Figure 5.25, Figure 5.27 and Figure 5.29 demonstrate the derivative of resistance with respect to sinkage, trim and flow rate, respectively.

Obviously, increasing the hull sinkage increases the total resistance of the hull (see Figure 5.24) but this is not necessarily the case for the trim angle (see Figure 5.26). The trim angle variation reveals that there is an optimum trim angle for the hull and depending on the bare hull trim angle, as well as the bow down or bow up trimming moment (most probably bow down) created by the waterjet system, the hull resistance may increase or decrease in self-propulsion.

75

Figure 5.24 Resistance variations against sinkage variations for ATHENA at *Fn*=0.6.

Figure 5.25 Resistance derivative with respect to sinkage for ATHENA at *Fn*=0.6.
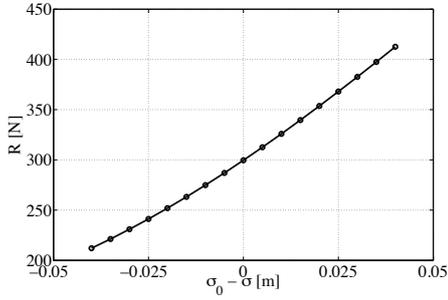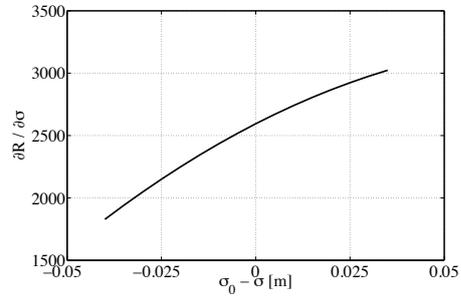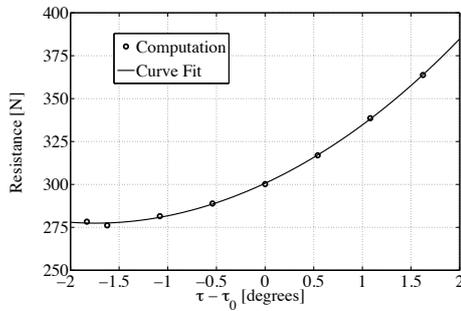

Figure 5.26 Resistance variations against trim angle variations for ATHENA at *Fn*=0.6.
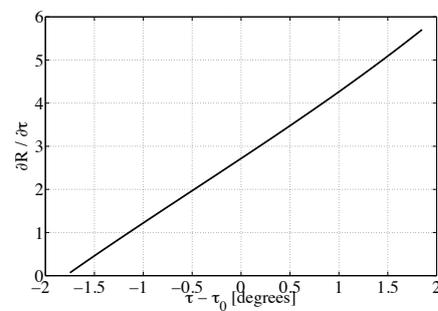
Figure 5.27 Resistance derivative with respect to trim angle for ATHENA at *Fn*=0.6.
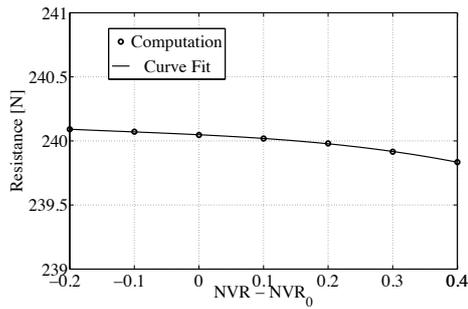
Figure 5.28 Resistance variations against NVR for ATHENA at *Fn*=0.6.
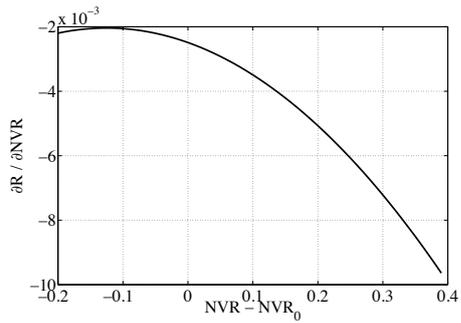
Figure 5.29 Derivative of the resistance with respect to NVR for ATHENA at *Fn*=0.6.

The optimum trim angle for a hull is closely related to the optimum transom area of that hull. As mentioned by Larsson and Raven [45], there is an optimum transom area for transom-stern hull types which increases with speed (Figure 5.30). The ratio A_{tr}/A_m given in Figure 5.30 is the ratio of the optimum transom area of the hull at rest, A_{tr}, to the maximum sectional area, A_m. According to the optimum values provided for the transom area in this figure, one may investigate whether the waterjet system trimming moment and sinking force helps to approach the optimum value or cause the transom area to move away from the optimum value. The last term of Equation (5-1) shows the impact of local flow change on the resistance increment. In order to obtain this term, it becomes necessary to fix the sinkage and trim angle of the self-propelled hull to those from the bare hull and set the flow rate to that obtained from the self-propulsion at a certain Froude number. Comparing the resistance change between the bare and self propelled hull with the fixed sinkage and trim angle reveals that for the self-propelled hull with a fixed sinkage and trim angle, the hull resistance is almost independent of the flow rate and the slope of the curve is almost zero (see Figure 5.28 and Figure 5.29).
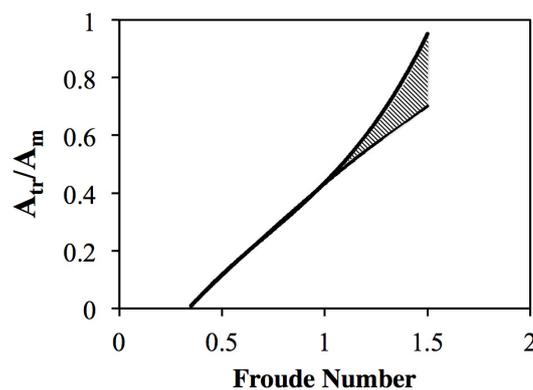
Figure 5.30 Optimum transom area vs. Froude number (extracted from [45])

With the derivatives of the resistance in hand, one may obtain the contribution of the terms in Equation (5-1). For this purpose, the values of $\frac{\partial R}{\partial \sigma}$ and $\frac{\partial R}{\partial \tau}$ can be taken from the curves provided in Figure 5.25 and Figure 5.27 at the point where the sinkage and trim of the self-propelled hull is the same as the bare hull. Then, multiplying these derivatives by the actual sinkage and trim change between the self-propelled hull and the bare hull (Figure 4.22 and Figure 4.21), the contribution of sinkage and trim to the resistance increment is obtained. The completed values of the resistance increment due to sinkage and trim for the R/V ATHENA hull at $Fn=0.6$ are given in Table 5.6.

As mentioned earlier, one can split the effect of the local flow change into wave making and viscous resistance. Table 5.6 shows the components of the local flow change, which contribute to the resistance increment. The wave making resistance is split into two components, where the first one is due to the change in wave pattern. This change is displayed in Figure 5.9, where it is seen that the wave trough is becoming deeper due to the suction. The second component is the effect on the transom clearance. Since the Froude number 0.6 for Athena is well above the critical value there is no effect of the difference in critical values between the bare hull and the self-propelled hull. There might be an effect of the interaction between the jet and the wave, but even this is unlikely at this relatively high Froude number for ATHENA. The value for his component is likely to be negligible, but it is marked as not estimated.

Table 5.5 Resistance increment due to the sinkage and trim for R/V ATHENA at *Fn*=0.6

$\frac{\partial R}{\partial \sigma}(Q,0,0)d\sigma$	$\frac{\partial R}{\partial \tau}(Q,0,0)d\tau$
+21.9	-0.1

Table 5.6 Components of the local flow change which contribute to the resistance increment for R/V ATHENA at *Fn*=0.6

Local Flow ($\Delta R(Q,0,0)$): +1.6			
Wave making resistance: +9.3		Viscous resistance: -7.7	
Wave pattern: +9.3	Transom clearance: not estimated	Missing intake area: -7.2	Boundary layer change: not estimated

* All resistance components given in the table are in Newton.

The viscous resistance change due to the local flow change is obtained by comparing the viscous resistance of the hull with or without intake. The missing surface at the intake opening for the hull with the ducting channel, results in a smaller viscous resistance, and as can be seen in the table this reduction accounts for almost the entire viscous resistance drop. The contribution from the changed boundary layer should thus be very small. It has not been estimated in the present work, but this should be done in further work. In general, one may conclude that there is some minor change in the wave making resistance and viscous resistance of the hull caused by the local flow change. These components are of the same order but have different signs. Consequently, they almost cancel each other and the total effect of the local flow change on the resistance increment becomes very small.

Concluding the results given in Table 5.5 and Table 5.6, the total resistance increment of the hull is obtained as follows:

78

$$\Delta R_{estimation}(Q, d\sigma, d\tau) = \frac{\partial R}{\partial \sigma}(Q, 0, 0)d\sigma + \frac{\partial R}{\partial \tau}(Q, 0, 0)d\tau + \Delta R(Q, 0, 0)$$

$$= \quad +7.8 \quad\quad - 0.1 \quad\quad\quad + 1.6 \quad\quad\quad = \quad 9.3 \ [N]$$

This is an estimation of the hull resistance increment and can be compared with the computation resistance increment obtained from pressure jump theory in Section 4.4.2. The computed bare hull and self-propelled hull resistance are 293.0 and 304.2 N, respectively. Thus the computational resistance increment can be obtained by subtracting these two values as follows:

$$\Delta R_{direct\ simulation} = R_{sp} - R_{bh} = 304.2 - 293.0 = 11.2 \ [N]$$

Comparing the estimated resistance increment and the computed resistance increment via pressure jump method indicates that there is a decent correspondence of the estimated ΔR with the computed one. Since the estimation of the resistance increment is based on the independency of the hull sinkage, trim and local flow changes, the difference between the obtained resistance increments might be related to non-linear relations between the three mentioned effects, but it is more likely that the numerical accuracy of the value from the direct simulation is too low. This small value is calculated by subtracting two large numbers, which reduces the numerical accuracy. But in general the estimated resistance increment suggests that the assumption of linear relation of the hull sinkage, trim and local flow changes on the resistance increment seems reasonable. Therefore, the relative magnitudes should also be reasonable, and it may be concluded that the sinkage has by far the largest influence on the resistance for this case, followed by the influence of the local flow change.

5.3.3 Estimation of the Difference between Net Thrust and Gross Thrust

The exit drag for R/V ATHENA at a Froude number of 0.6 is zero, since the jet exit is well in front of the stern wave. There may however be a significant intake drag. A direct computation based on the definition (or possibly based on the different contributions) cannot be made using the main tools of the present investigation: potential flow and boundary layer methods, but it may well be done using a viscous flow method of the RANS type. This should be done in further work.

Since a direct computation cannot be made of the intake drag, an indirect estimation can be made by comparing the computed net and gross thrusts for ATHENA using the pressure jump method. For a Froude number of 0.6 the net thrust is 280 N, while the gross thrust is 306 N. The difference is thus 26 N, or 8.5% of the gross thrust. This is a surprisingly large number, which must be treated with

caution. Again, we have a difference between two large numbers obtained in completely different ways.

5.4   Possibilities for a Negative Thrust Deduction

Investigation of the possibility of a negative thrust deduction fraction is achievable through analysis of the hull resistance increment and its intake drag. These two effects have been extensively discussed in the previous sessions of this chapter. In this session, all the parameters, which may have impact on the thrust deduction fraction of a hull, will be further analyzed to explore the possibilities of a negative thrust deduction.

The main effective parameters on the resistance increment of a hull are sinkage, trim and local flow variations. In section 5.1 it was shown that, following the ITTC proposed procedure, it is only the intake-induced pressure, which has a major effect on the sinkage and trim angle of the self-propelled hull. The intake-induced pressure causes the hull to sink more (Figure 5.19 and Figure 5.20), which obviously increases the hull resistance. Moreover, it was shown that the intake-induced pressure mostly exerts a bow down trimming moment on the hull except for short lengths of the hull after the intake trailing edge (Figure 5.22 and Figure 5.23). In case of a short hull length after the intake trailing edge comparing to the longer one, some part of the high-pressure zone locates outside the hull, which makes the bow-down trimming moment smaller.

The most important effect of the combined sinkage and trim change is the change transom submergence. There exists a correlation between the hull transom submergence, its effective waterline length and its resistance. Increasing the submergence of the (dry) transom increases the hull resistance, due to the lost hydrostatic pressure on a larger area, while the increase in effective waterline length goes in the opposite direction and decreases the hull resistance. As a result of both effects there is an optimum transom area for each Froude number, and this is given in Figure 5.30. If the combination of sinkage and trim (changes) causes the transom size to approach the optimum, the resistance will decrease, and vice versa. Thus, if the hull is optimized for bare hull conditions, it will not be optimum in self-propulsion and the resistance will increase. This will contribute to a positive thrust deduction. On the other hand, if the hull is not optimized in bare hull conditions, by chance the optimum may be approached in self-propulsion. Then there is a chance of a negative thrust deduction, but this is only due to the bad original design. It is obviously best to optimize the hull for self-propulsion.

Preliminary studies indicate that almost 90% of the HAMILTON hull is associated with the transom stern resistance, which shows the importance of the transom

submergence for this specific hull. Small changes in the transom submergence of the HAMILTON jet boat will have a large impact on the resistance.

Besides sinkage and trim, local flow changes also contribute to the hull resistance increment. The change in the flow filed in vicinity of the waterjet intake alters wave pattern. Since, almost always, the waterjet suction lowers the wave trough in this region this effect increases the hull resistance. In addition to the wave pattern change, ingestion of flow into the waterjet system makes the transom wave steeper. This will delay in the Froude number, at which the hull transom clears. Since the resistance increases considerably just when the transom clears, due to the lost hydrostatic pressure, a large resistance difference may be obtained in the Froude number range where the self-propelled hull transom is still wet, but the bare hull transom is cleared and no hydrostatic pressure is exerted on it. This effect may result in large negative thrust deduction fractions.

Moreover, the interaction of the discharged jet with a steep transom wave may cause splashing, which can partially fill in the wave trough behind the hull transom (See Figure 5.10). This effect will increase the transom hydrostatic pressure and reduce the transom drag. Since the resistance of the HAMILTON jet boat is mainly associated with the transom stern resistance, even very little filling of the trough may change the hull resistance significantly which may result in a negative thrust deduction fraction.

The next effect, which contributes to the thrust deduction fraction, is the intake drag. van Terwisga [10] indicates that the intake drag is negligible except at hump speed. In the current work, a direct computation of the intake is not accomplished due to the limitation of the main employed tools, potential flow and boundary layer methods, but instead an indirect estimation of the intake drag is made by comparing the computed net and gross thrusts for ATHENA using the pressure jump method. Probably, this over-predicts the intake drag. According to the uncertainty of the employed method, further study of the intake drag employing a viscous solver is required. It is unlikely that this effect can contribute to the negative thrust deduction

 In conclusion, there are two main reasons for negative thrust deduction. First, the combination of sinkage and trim changes that may cause the transom submergence to get closer to the optimum in self-propulsion and second, the local flow effects on transom clearance, i.e. the delayed critical Froude number and the effect of splashing.

6 Conclusion and Future Work

6.1 Conclusion

As seen in Chapter 2, the motivation for this work has been twofold: to develop better understanding of the physics behind the waterjet/hull interaction, in particular the negative thrust deduction phenomenon, and to develop a fast and sufficiently accurate method for estimating the gross thrust of a waterjet driven hull. Since the method would be a useful tool in the investigation of the physics it was developed first. In this report it has been named the Pressure Jump Method.

The Pressure Jump Method relates the hull resistance to the gross thrust and may be used in combination with both potential flow/boundary layer methods and more advanced viscous flow methods, for instance of the RANS type. In the present work the potential flow/boundary layer approach has been used.

It is extremely difficult to find high quality measured data for validation, but in the present work the data from an experimental campaign within the 24th ITTC Specialist Committee on Waterjets have been used. The data were obtained for the research vessel ATHENA and contain considerable scatter, which reduces the reliability of the validation.

Due to the limitations of the potential flow assumption, there are some deviations between the computed and measured resistance, sinkage and trim. The former is however relatively accurately predicted using a correction technique, and is spite of the limitations the predictions of inlet velocity ratio, nozzle velocity ratio, gross thrust and thrust deduction are all within the experimental scatter. It should be noted that the predicted thrust deduction fraction is positive, as well as all the measured data in model scale.

A mapping of the waterjet/hull interaction effects has been presented in the form of a flow chart. This chart includes all effects envisioned to relate bare hull resistance and gross thrust. Its main components are sinkage, trim, local effects, intake drag and exit drag. All are discussed in the report. The sinkage, trim and local flow effects are subdivided into components, and based on an analysis of these components the following conclusions may be drawn:

1. There is no sinkage or trim for a waterjet in free-stream conditions, i.e. for a waterjet fitted to an infinitely large flat plate and ejecting the flow horizontally. This is under the condition of infinitely deep water.
2. The waterjet induced pressure on the hull increases the sinkage, which increases resistance

82

3. The influence of the waterjet-induced pressure on the trimming moment depends on the distance between the waterjet intake and the transom, and on the position of the centre of floatation. For most hulls a bow-down moment is generated, but if the intake is far aft, a moment in the other direction may be generated. Also, if the hull is very long, with a centre of floatation at a large distance from the intake, the moment may be bow-up.

4. An inclination of the waterjet nozzle always induces a bow-down effect, as does the resistance/thrust couple.

5. There is an optimum trim angle for the hull where the resistance is minimum. This is normally obtained where the transom has an optimum size. An increased trim may increase or decrease the resistance depending on the position on the resistance/trim curve relative to the optimum trim angle. The trim angle is one candidate for reducing the resistance, unless the hull has been optimized for self-propulsion.

6. Wave resistance normally increases due to deepening of wave trough at the stern

7. The transom clearance is influenced by the waterjet in two ways: the critical Froude number for transom clearance is increased and the splashing of the waterjet into the stern wave may (partly) fill the trough behind the transom, thus decreasing the transom resistance. The transom clearance effect is the other important factor that may reduce resistance and cause a negative thrust deduction.

8. The viscous resistance decreases due to the missing surface covering the intake opening, but it may increase somewhat due to the changes in the boundary layer around the intake.

6.2 Future Work

According to the predicted sinkage, trim and resistance of the hull in potential flow, neglecting the viscous effects caused some error in computed results. Redoing the same calculations employing the Pressure Jump Method in a viscous flow solver capable of two-phase flow modelling may provide additional information on the flow features around the hull and may also assist in obtaining more exact hull equilibrium position and resistance.

Studying the intake drag seems to be key to investigating the thrust deduction phenomenon of the waterjet propelled vessels. This study requires capturing the exact stream tube shape. A RANS solver may be more suitable and efficient for this purpose than a potential flow solver.

Moreover, studying the typical thrust deduction factor variation against the Froude number, there may be an abrupt change of the hull sinkage, trim and, consequently, its thrust deduction factor at speed ranges where the transom starts to clear. An active waterjet may postpone the clearance of the transom, which in turn influences hull resistance. Besides, the interaction of the discharged jet with the stern wave may also influence the clearance of the transom. Investigating both these phenomena and applying a viscous flow solver along with two-phase flow modelling may reveal additional information about the hull resistance variation close to the transom clearance speed.

At higher Froude numbers, a cavitating flow starts to emerge on the region close to the intake tangency point of the hull, which possibly is an important effect that may alter hull resistance. Investigating the impact of cavitation on hull resistance for high-speed hulls may be taken into account for future studies.

Appendices

Appendix A.   Marine Waterjet Development History

Some Historical Events Pertinent to Marine Waterjet Development History[46]

287-212 BC	Archimedes	Axial Water Pump
1452-1519	Leonardo Da Vinci	Axial Water Pump, Screw Propulsion
1631	David Ramsey	Patented Steam Waterjet Ship Propulsion
1642-1727 (1687)	Isaac Newton	Isaac Newton in his *Philosophiae naturalis principia mathematica* formulated the laws of science that are applicable to Ramsey's idea
1661	Toogood and Hayes	Patent for Archimedean Screw WJ
1680	Robert Hooke	Archimedean Screw Propeller
1775	Benjamin Franklin	Proposal for Waterjet Propelled Boat
1736-1819	James Watt	Reciprocating and Rotary Steam Engins
1782	James Rumsey	Waterjet Propelled 80 ft Ferry Boat (Potomac)
1787	Kempelen	Steam Turbines
1791	Barber	Patented Gas Turbine
1802	William Symington	Charlotte Dundas Steam Tug (Clyde)
1807	Robert Fulton	Clemont Steamship (Hudson)
1812	Henry Bell	Steamship Comet (Clyde)
1836-1845	Francis Pettit Smith	Screw Propellers, England
1840's	John Ericsson	Marine Propellers (Including Contra-Rotating), Sweden/USA
1853	John Ruthven	Waterjet Ship Enterprise (Not Successful)
1853	Seydell	Waterjet Ship Albert (Successful) (Oder)
1863	British Admiralty	Waterjet Ship Nautilus, 10 kt (Thames)
1863	British Admiralty	Waterjet Ship Waterwitch Versus Viper
1870	C.M. Ramus	Planning Boat Rocket Propulsion
1878	Swedish Government	Comparative Trials Waterjet and Propeller
1880	Thorneycroft J1	Pump-Jet Propulsion (Exterior)
1894	Royal National Lifeboat Institution	Waterjet Lifboat
1932	First Riva Calzoni Waterjet	
1959-1967	Donald Cambell	Bluebird, Gas Turbine Jet Propulsion
1952	Etablissements Billiez	Waterjet Ferry (France)
1954	First Hamilton Waterjet	New Zealand's Rivers
1968	First KaMeWa Waterjet	Mixed Flow Pump Waterjet
1968-1972	Tucumcari (PGH-2)	Boeing/Cenrifugal Pump
1971-1980	SES 100A	74 kt (1978) Inducer Pump Waterjet
1971-1983	SES 100B	92 kt (1977) Surface Piercing Propellers
1973-1978	2K/3KSES	Most Powerful Waterjet Development
1974-present	PHM	Boing/ALRC Inducer/Mixed Flow, 2 Speed Coaxial Shaft Pumps
1974-present	Jetfoil	Boeing/Kawasaki Inducer/ Axial Pumps
1989	Riva Calzoni	Atlantic Challenger Waterjet
1990	SES 200	Waterjet Conversion
1991	KaMeWa 180 SL1	Largest Current Waterjet Built
1992	SEC SES	Largest Waterjet Ship
1992	Yamato	First MHD Waterjet Ship
1992	Destriero	Atlantic Speed Record with KaMeWa Waterjets

Appendix B. Wave Making Resistance Correction

Table b. AMECRC systematic series

Model	L/B	B/T	C_b	$WSA[\text{m}^2]$	Δ [kg]	$L/\nabla^{1/3}$
1	8.00	4.0	0.396	0.3149	6.321	8.649
2	6.51	3.5	0.395	0.3850	11.455	7.100
3	8.00	2.5	0.447	0.3794	11.454	7.074
4	8.00	4.0	0.447	0.3056	7.158	8.274
5	4.00	4.0	0.395	0.6297	25.344	5.444
6	8.00	2.5	0.395	0.3554	10.123	7.393
7	4.00	2.5	0.396	0.7111	40.523	4.649
8	4.00	2.5	0.500	0.7463	51.197	4.300
9	8.00	2.5	0.500	0.3732	12.804	6.817
10	8.00	4.0	0.500	0.3136	8.003	7.990
11	4.00	4.0	0.500	0.6272	32.006	5.031
12	8.00	3.3	0.497	0.3354	9.846	7.442
13	8.00	3.3	0.450			6.362
14	6.00	4.0	0.500	0.4180	14.204	6.593

* All models are 1.6 m in length

Table a. Constants to be used for obtaining resistance correction factor

a_1	-14.741
a_2	8.353
a_3	6.569
a_4	-7.103
a_5	-41.182
a_6	70.842
a_7	-44.422
a_8	-34.315
a_9	38.226
a_{10}	226.876
a_{11}	-106.445
a_{12}	87.905
a_{13}	67.534
a_{14}	-78.547
a_{15}	-473.974
a_{16}	52.252
a_{17}	-76.289
a_{18}	-58.507
a_{19}	71.958
a_{20}	441.525
a_{21}	-1.258
a_{22}	24.716
a_{23}	18.962
a_{24}	-24.703
a_{25}	-156.221

Appendix C. HAMILTON Jet Test Boat

The main particulars of the full-scale test boat at the parent condition Δ_0, LCG_0 are presented in the following [10].

| Description	Symbol	Magnitude	Unit
Length between perpendiculars (Fr. 1-8)	L_{PP}	7.27	m
Length on waterline	L_{WL}	6.27	m
Hull beam at draught moulded at mid-ship	B	2.226	m
Draught moulded on FP	T_F	0.386	m
Draught moulded on AP	T_A	0.424	m
Displacement volume moulded	∇	2.798	m^3
Displacement mass in sea water	Δ	2.868	t
Wetted surface area bare hull at rest	S	13.264	m^2
LCB position aft of frame 8	LCB	4.58	m
Slenderness ratio	$L_{PP}/\nabla^{1/3}$	5.16	-
Length to beam ratio	L_{PP}/B	3.27	-
Beam to draught ratio	B/T_M	5.50	-
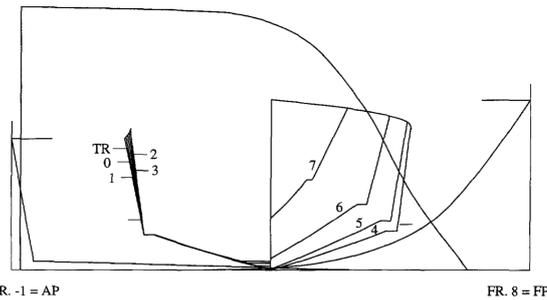
Figure 6.1 Body plan, stem and stern profiles and sectional area curve of model
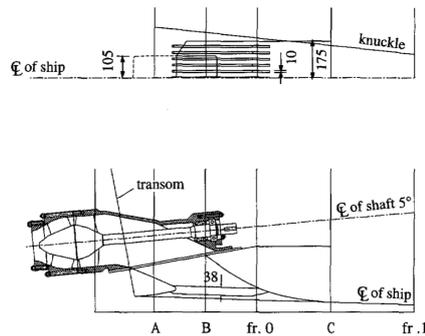

Figure 6.2 Waterjet intake opening and ducting geometry
(Dimensions are given in millimetres)

Nomenclatures

A: control surface
A_H: water plane area
A_I: intake opening area
$A_{impeller}$: impeller area
A_m: hull maximum sectional area
A_{nozzle}: nozzle discharge area
A_{tr}: hull transom area
B: hull beam
C_b: block coefficient
C_F: total friction coefficient
C_L: lift coefficient
CoF: centre of floatation
c_p: local pressure coefficient
C_p: pressure coefficient
CV: control volume
C_W: wave-making resistance coefficient obtained from pressure integration
C_{WTWC}: wave-making resistance obtained from the transverse wave cut method
D_e: exit drag
D_i: intake drag
$D_{impeller}$: impeller diameter
D_{nozzle}: nozzle diameter
F: force vector
F_D: ducting channel lift force
F_H: lift force on the flat plate hull in free-stream condition
F_I: lift force on the imaginary intake covering the hull opening
Fn: Froude number
F_O: lift force on the outer domain in free-stream condition
F_S: lift force on the entire flat surface in free-stream condition
F_p: pump force vector
g: gravitational acceleration
GM_L: hull metacentric height
H: flow head
h: height of the capture area
i, j, k: tensor indices denoting the ordinates
IVR: intake velocity ratio at the capture area
IVR_i: intake velocity ratio at the rectangular intake area on hull
JVR: jet velocity ratio
KCW: correction factor of the wave making resistance obtained from pressure integration
LCB: longitudinal centre of buoyancy
LCG: longitudinal centre of gravity
LOW: waterline length
Lpp: length between perpendiculars

m: hull mass displacement
M: momentum flux vector
M_y: moment about the y-axis
n: normal unit vector
NVR: nozzle velocity ratio
n_λ: number of panels per characteristic wavelength
p: time averaged pressure
P_{after}: pressure after the impeller disk
p_{atm}: atmospheric pressure
P_{front}: pressure before the impeller disk
p_{wop}: pressure after the impeller disk without pressure jump
Q: volume flow rate
R: jet diameter
r: resistance increment
R: resistance vector
R_A: rope force
R_{bh}: bare hull resistance
R_D: ducting channel resistance
R_H: hull resistance
R_N: nozzle resistance
Rn: Reynolds number
R_{sp}: self-propelled hull resistance
R_{TWOP}: total resistance of the waterjet/hull system without pressure jump
S: control surface
T: hull draught
t: total thrust deduction fraction
T_g: gross thrust vector component in x-directon
t_j: jet thrust deduction fraction
T_{net}: net thrust vector component in x-directon
t_r: hull thrust deduction fraction
u: velocity vector
u_∞: undisturbed velocity
u_ϕ: tangential component of velocity vector
V: control volume
w: width of ducting channel intake
w_{capt}: width of the capture area
x, y, z: Cartesian earth fixed coordinates
β: momentum flux correction factor
∇: displacement volume
Δ: displacement mass
δ_{ij}: Kronecker delta
Δp: pressure jump through impeller
ΔR: resistance increment
θ: shaft line angle with horizon ($\theta = \theta_n + \tau$)
θ_n: nozzle inclination angle with horizon
ρ: density of fluid
σ: hull sinkage

σ_{ij}: total mean stress tensor
τ: hull trim angle
τ_{ij}: shear stress tensor
ϕ: momentum flux vector
$\vec{T}_g$: gross thrust vector in ship-fixed coordinates
$\vec{T}_{net}$: net thrust vector in ship-fixed coordinates

Subscripts:
bh: bare hull
est: estimated
EW: entrained water
M: model scale
n: nozzle
RT: resistance/thrust
S: ship
sp: self-propulsion
0: free-stream condition
∞: undisturbed

References

[1] J. Raithby, *The statutes relating to the admiralty, Navy, shipping, and navigation of the United Kingdom, from 9 Hen. III to 3 Geo. IV inclusive*. Printed by George E. Eyre and Andrew Strahan, Printers to the King's most Excellent Majesty, 1829.

[2] W. Bennet, *Patents for inventions. Abridgments of the specifications; Marine Propulsion(excluding sails)*. Printed by George E. Eyre and William Spottiswoode, Printers to the Queen's most Excellent Majesty, 1858.

[3] S. M. Roy, "The Evolution of the Modern Waterjet Marine Propulsion Unit," in *International Symposium if Waterjet Propulsion, RINA*, 1994.

[4] J. T. Flexner, *Steamboats come true : American inventors in action*. New York: Viking Press, 1944.

[5] J. Schult, *Curious Boating Inventions*. London: Elek, 1974.

[6] H. E. Saunders, "Hydrodynamics in Ship Design," 1957, pp. 648-649.

[7] H. L. Jones, Jr. , Paul, Harman, "Toy Boat," U.S. Patent 19936701935.

[8] J. L. Allison, A. J. Bencnel, J. G. Purnell, J. J. Gorski, J. G. Hoyt III, and M. B. Wilson, "Research in Waterjet Inlet, Hull and Jet Interactions," in *Waterjet Propulsion III*, 2001.

[9] N. W. H. Bulten, "Numerical Analysis of a Waterjet Propulsion System," Eindhoven University of Technology, 2006.

[10] T. van Terwisga, "Waterjet-Hull Interaction," Delft Technical University, 1996.

[11] J. Carlton, *Marine Propellers and Propulsion*, Second Edi. Elsevier Ltd., 2007.

[12] C. Kruppa, C., Brandt, H., Östergaard, "Wasserstrahlantriebe für Hochgeschwindigkeitsfahrzeuge," in *Jahrbuch der STG 62*, 1968, pp. 228-258.

[13] J. G. Purnell, "The Performance Gains of Using Wide Flush Boundary Layer Inlets on Water-Jet Propelled Craft," Annapolis, 1976.

[14] K. Alexander, H. Coop, and T. van Terwisga, "Waterjet-Hull Interaction Recent Experimental Results," in *SNAME Transaction*, 1994, pp. 87-105.

[15] G. Dyne and P. Lindell, "Waterjet Testing in the SSPA towing Tank," in *International Symposium if Waterjet Propulsion, RINA*, 1994.

[16] J. L. Roberts and G. J. Walker, "Performance of waterjet propulsion system with boundary layer ingestion," in *Twelfth Australian Fluid Mechanics Conference*, 1995, pp. 271-274.

[17] T. van Terwisga and K. V. Alexander, "Controversial issues in waterjet-hull interaction," in *International Conference on Fast Sea Transportation, FAST '95*, 1995, pp. 1235–1253.

[18] A. Johansson, "Trim Effect on High-Speed Craft due to Waterjet-Hull Interaction," KTH Royal Institute of Technology, 1995.

[19] J. L. Roberts, "The Influence of Hull Boundary Layers on Waterjet Intake Performance," no. February, 1998.

[20] G. Dyne, C. Kruppa, B. Lamberti, and K. J. Minsaas, "Report of the Specialist Committee on Waterjets, 21st International Towing Tank Conference," 1996.

[21] P. Hu and M. Zangeneh, "CFD Calculation of the Flow Through a Water-Jet Pump," in *Waterjet Propulsion III*, 2001.

[22] T. van Terwisga et al., "The Specialist Committee on Validation of Waterjet Test Procedures: Final Report and Recommendations to the 23rd ITTC," 2002.

[23] J. L. Roberts, "The Influence of Hull Boundary Layers on Waterjet Intake Performance;," University of Tasmania, 1998.

[24] M. B. Wilson, C. Chesnakas, S. Gowing, A. J. Becnel, J. G. Punell, and J. G. Stricker, "Analysis of hull boundary layer velocity distributions with and without active waterjet inlets," in *Waterjet Propulsion 4*, 2004, pp. 29-37.

[25] N. Bulten and B. van Esch, "Review of Thrust Prediction Method Based on Momentum Balance for Ducted Propellers and Waterjets," *ASME Conference Proceedings*, vol. 2005, no. 41987, pp. 1621-1629, 2005.

[26] M. B. Wilson, S. Gowing, C. J. Chenakas, and C.-W. Lin, "Waterjet-Hull Interaction for Sealift Ships," in *International Conference on Marine Research and Transportation (ICMRT'05)*, 2005.

[27] J. O. Sherer and I. Mutnick, "Procedure for conducting a towing tank test of a waterjet propelled craft using Laser Doppler velocimetry to determine the momentum and energy flux," in *Proceedings of 26th ATTC*, 2001.

[28]   T. van Terwisga et al., "The Specialist Committee on Validation of Waterjet Test Procedures, Proceedings of the 24th ITTC," 2005.

[29]   D. S. Cusanelli, S. A. Carpenter, and A. M. Powers, "Axial Waterjet (AxWJ) Model 5662 and Mixed-Flow Waterjet (MMMWJ) Model 5662-1: Comparisons of Resistance and Model- Scale Powering with Propulsion Nozzle Designs," 2007.

[30]   S. D. Jessup, M. J. Donnelly, D. Fry, D. Cusanelli, and M. Wilson, "Performance Analysis of a Four Waterjet Propulsion System for a Large Sealift Ship," in *Proceedings of the 27th Symposium on Naval Hydrodynamics*, 2008.

[31]   T. Hino and K. Ohashi, "Numerical Simulation of Flow around a Waterjet Propelled Ship," in *First International Symposium on Marine Propulsors smp'09*, 2009.

[32]   M. KANDASAMY, S. KEAT OOI, P. CARRICA, and F. STERN, "Integral Force/Moment Waterjet Model for CFD Simulations," *Journal of fluids engineering*, vol. 132, no. 10.

[33]   T. Takai, "Simulation based design for high-speed sea lift with waterjets by high fidelity URANS approach," The University of Iowa, 2010.

[34]   J.-ming Ding and Y.-sheng Wang, "Research on flow loss of inlet duct of marine waterjets," *Journal of Shanghai Jiaotong University (Science)*, vol. 15, no. 2, pp. 158-162, Apr. 2010.

[35]   E. Methods, H. Speed, M. Vehicles, and P. P. Prediction, "ITTC – Recommended Procedures and Guidelines ITTC – Recommended Procedures and Guidelines Waterjet Propulsive Performance Prediction – Propulsion Test and Extrapolation," 2005.

[36]   A. Navale, J. George, and H. Iii, "The Specialist Committee on Validation of Waterjet Test Procedures Final Report and Recommendations to the 24th ITTC," vol. II, pp. 471-508, 2004.

[37]   F. M. White, *Fluid Mechanics*, Sixth. McGraw-Hill, 2008.

[38]   "SHIPFLOW." FLOWTECH AB, Gothenburg.

[39]   V. Höglund, "Validation and Correction of SHIPFLOW for Fast Hulls," Chalmers University of Technology, 2004.

[40]   S. HARRIES and D. SCHULZE, "Numerical investigation of a systematic model series for the design of fast monohulls," in *International Conference on Fast Sea Transportation, FAST '97*, 1997.

[41] T. van Terwisga et al., "The presentation for the report of the 24th ITTC Specialist Committee on; Validation of Waterjet Test Procedures," Edinburgh, 2005.

[42] K.-H. Kim et al., "Final Report and Recommendations to the 25th ITTC," in *Proceedings of 25th ITTC*, 2008.

[43] J. Allison, "Marine waterjet propulsion," in *Transactions - Society of Naval Architects and Marine Engineers*, 1993, vol. 101, pp. 275-335.